Complexes of vertebrate TMC1/2 and CIB2/3 proteins form hair-cell mechanotransduction cation channels

Arnaud P. J. Giese[1,#,*], Wei-Hsiang Weng[2,3,*], Katie S. Kindt[4], Hui Ho Vanessa Chang[5], Jonathan S. Montgomery[2,6], Evan M. Ratzan[7], Alisha J. Beirl[4], Roberto Aponte Rivera[4], Jeffrey M. Lotthammer[2], Sanket Walujkar[2], Mark P. Foster[2,3,6], Omid A. Zobeiri[8], Jeffrey R. Holt[7], Saima Riazuddin[1], Kathleen E. Cullen[9], Marcos Sotomayor[2,3,6] , Zubair M. Ahmed[1,10,11]

[1]Department of Otorhinolaryngology – Head & Neck Surgery, University of Maryland School of Medicine, Baltimore, MD, USA.

[2]Department of Chemistry and Biochemistry, The Ohio State University, Columbus, OH, USA.

[3]Biophysics Graduate Program, The Ohio State University, Columbus, OH, USA.

[4]Section on Sensory Cell Development and Function, National Institute on Deafness and Other Communication Disorders, National Institutes of Health, Bethesda, MD, USA.

[5]Department of Physiology, McGill University, Montreal, QC, Canada.

[6]Ohio State Biochemistry Program, The Ohio State University, Columbus, OH, USA.

[7]Departments of Otolaryngology and Neurology, F.M. Kirby Neurobiology Center, Boston Children's Hospital, Harvard Medical School, Boston, MA, USA.

[8]Department of Biomedical Engineering, McGill University, Montreal, QC, Canada.

[9]Departments of Biomedical Engineering, Neuroscience, and Otolaryngology and Head and Neck Surgery, Johns Hopkins University School of Medicine, Baltimore, MD, USA.

24 [10]Department of Biochemistry and Molecular Biology, University of Maryland School of
25 Medicine, Baltimore, MD, USA.
26 [11]Department of Ophthalmology and Visual Sciences, University of Maryland School of
27 Medicine, Baltimore, MD, USA.
28 [#]Current address: SENSORION SA, Montpellier, France.
29 *Contributed equally.
30 Correspondance:
31 Emails: sotomayor.8@osu.edu; zmahmed@som.umaryland.edu
32
33 Keywords: CIB2, CIB3, mechanotransduction, TMC1, TMC2, Vestibular hair cells

Abstract

Calcium and integrin-binding protein 2 (CIB2) and CIB3 bind to transmembrane channel-like 1 (TMC1) and TMC2, the pore-forming subunits of the inner-ear mechano-electrical transduction (MET) apparatus. Whether these interactions are functionally relevant across mechanosensory organs and vertebrate species is unclear. Here we show that both CIB2 and CIB3 can form heteromeric complexes with TMC1 and TMC2 and are integral for MET function in mouse cochlea and vestibular end organs as well as in zebrafish inner ear and lateral line. Our AlphaFold 2 models suggest that vertebrate CIB proteins can simultaneously interact with at least two cytoplasmic domains of TMC1 and TMC2 as validated using nuclear magnetic resonance spectroscopy of TMC1 fragments interacting with CIB2 and CIB3. Molecular dynamics simulations of TMC1/2 complexes with CIB2/3 predict that TMCs are structurally stabilized by CIB proteins to form cation channels. Overall, our work demonstrates that intact CIB2/3 and TMC1/2 complexes are integral to hair-cell MET function in vertebrate mechanosensory epithelia.

49 **Introduction**

50 The vertebrate senses of hearing and balance depend on the process of mechano-
51 electrical transduction (MET) in inner-ear hair cells. This process is initiated when mechanical
52 forces from sound waves and head movements deflect specialized mechanosensory projections
53 at the apical surface of hair cells, known as stereocilia (reviewed in Fettiplace, 2017; Frolenkov
54 et al., 2004; Gillespie and Müller, 2009). Deflections of stereocilia result in tensioning of the
55 extracellular tip links that convey mechanical force to the MET channels. Mature tip links are
56 heterotetrameric filaments composed of cadherin 23 (CDH23) and protocadherin 15
57 (PCDH15) (Ahmed et al., 2006; Kazmierczak et al., 2007; Siemens et al., 2004; Sotomayor et
58 al., 2012). In mammalian auditory hair cells, MET channels are localized at the PCDH15 end
59 of the tip link (Beurg et al., 2009). Significant progress in our understanding of MET has been
60 recently made by identifying the transmembrane channel-like proteins 1 and 2 (TMC1 and
61 TMC2) as the pore-forming subunits of the MET channel (Kawashima et al., 2011; Pan et al.,
62 2018). In hair cells, two other transmembrane proteins, LHFPL5 and TMIE, are essential for
63 sustained hearing. LHFPL5 binds to PCDH15 and may regulate force transmission to TMC1
64 and TMC2 (Qiu et al., 2023; Xiong et al., 2012). TMIE also interacts with TMC1/2 and
65 regulates unitary conductance and ion selectivity of the MET channels (Cunningham et al.,
66 2020; Naz et al., 2002). Interestingly, MET currents can still be recorded from hair cells lacking
67 LHFPL5 or TMIE, suggesting that neither are essential for channel function (Fettiplace et al.,
68 2022).

69 We previously showed that calcium (Ca^{2+}) and integrin-binding protein 2 (CIB2), and
70 the closely related CIB3, interact with TMC1/2 (Giese et al., 2017). Furthermore, we also
71 demonstrated that CIB2 is essential for MET function in auditory hair cells (Giese et al., 2017).
72 Recessive variants of CIB2 predominantly cause nonsyndromic DFNB48 hearing loss in

humans (Booth et al., 2018; Michel et al., 2017; Riazuddin et al., 2012; Seco et al., 2016; Wang et al., 2017). Similarly, recessive alleles of *Cib2* cause hearing loss in mice but no vestibular deficits (Giese et al., 2017; Michel et al., 2017; Wang et al., 2017). CIB2 belongs to a family of four closely related proteins (CIB1-4) that have similar structural domains and have partial functional redundancy (Huang et al., 2012). Wang and co-authors investigated the function of *Cib1* in cochlear hair cells through generation of a knockout strain and concluded that although *Cib1* is expressed in the mouse cochlear hair cells, loss of CIB1 protein did not affect auditory function (Wang et al., 2017). A recent study demonstrated that while CIB2 is essential for proper localization of TMC1/2 at the tips of auditory hair cell stereocilia, CIB3 can restore MET currents in cochlear hair cells lacking CIB2 (Liang et al., 2021). The same study reported a crystal structure of a TMC1 intracellular linker in complex with CIB3, which suggests that CIB2/3 proteins are likely to be auxiliary subunits of hair cell MET channels (Liang et al., 2021).

Previous work on CIB proteins primarily focused on auditory hair cells, leaving open the question of whether they play a role in vestibular function. This question was addressed in part by another recent study that reported vestibular deficits in mice lacking both CIB2 and CIB3 (Wang et al., 2023). However, whether CIB2/3 can function and interact with TMC1/2 proteins across sensory organs, hair-cell types, and species is still unclear. Here we provide further evidence that CIB2 and CIB3 are indeed evolutionary conserved and functionally redundant components of the vertebrate transduction apparatus necessary for MET channel activity in mouse vestibular hair cells, as well as in zebrafish mechanosensory epithelia. Moreover, based on our structural analyses and simulations, we propose that CIB2 and CIB3 are required for stabilization and channel function of the MET proteins TMC1 and TMC2.

97 **Results**

98 **CIB2 and CIB3 are expressed in mouse vestibular hair cells**

99 We and others previously demonstrated that CIB2 is essential for MET in auditory hair
100 cells (Giese et al., 2017; Michel et al., 2017; Wang et al., 2017). In contrast to auditory hair
101 cells, we found that the vestibular hair cells in *Cib2*$^{KO/KO}$ mice have intact MET. We assessed
102 MET via uptake of FM 1-43 (Figure 1A), a styryl dye that permeates into hair cells through
103 functional MET channels (Meyers et al., 2003), indicating that there may be another CIB
104 protein playing a functionally redundant role. Bulk RNA sequencing revealed that all four
105 members of the *Cib* family are expressed in mouse inner ear tissues (Figure 1B). However,
106 when assessed by single cell RNA sequencing analysis, only *Cib2* and *Cib3* are expressed in
107 immature hair cells in the mouse utricle (Figure 1C), a vestibular sensory organ required to
108 detect linear acceleration (McInturff et al., 2018). Further, we find that the expression of *Cib2*
109 and *Cib3* is maintained in mature type 1 and type 2 utricular hair cells (Figure 1C). We also
110 examined the expression of *Tmc1* and *Tmc2* in utricular hair cells and found that in immature
111 hair cells *Tmc1* is highly expressed, while *Tmc2* expression is low (Figure 1C). *Tmc2*
112 expression increases during development and becomes comparable to *Tmc1* in both type 1 and
113 type 2 hair cells upon maturation (Figure 1C). CIB2 and CIB3 have been reported to interact
114 with TMC1/2, and CIB2 is essential for auditory hair cell MET (Giese et al., 2017; Liang et
115 al., 2021). The co-expression of *Cib2* and *Cib3* in developing and mature vestibular hair
116 bundles, and the ability of CIB2/3 to interact with TMC1 and TMC2, all make them attractive
117 candidates to regulate MET function in vestibular hair cells.

118

119 **CIB3 is not required for hearing function in mice**

120 To evaluate whether CIB3 regulates MET function both in auditory and vestibular hair

121 cells, we generated *Cib3* knockout (*Cib3*^{KO}) mice using CRISPR/Cas9 technology (Figure 1D).
122 An indel in exon 4 of *Cib3* was introduced leading to a nonsense mutation (p.Asp54*), thus
123 causing a loss of allele function (Figure 1E-F). We first characterized hearing function in
124 *Cib3*$^{KO/KO}$ and control littermate mice at P16 by measuring auditory-evoked brainstem
125 responses (ABRs). Normal ABR waveforms and thresholds were observed in wild-type and
126 *Cib3*$^{KO/KO}$ mice, indicating normal hearing (Figure 2A-B). Next, we investigated if there was a
127 functional redundancy between CIB2 and CIB3 in auditory hair cells. For this analysis, the
128 *Cib3*^{KO} allele was introduced into the *Cib2*^{KO} background. Similar to what has been previously
129 reported in *Cib2*$^{KO/KO}$ mice (Giese et al., 2017; Michel et al., 2017; Wang et al., 2017), the
130 *Cib2:Cib3* double knockout (*Cib2*$^{KO/KO}$*;Cib3*$^{KO/KO}$) mice were also profoundly deaf. The
131 *Cib2*$^{KO/KO}$*;Cib3*$^{KO/KO}$ mice did not respond to click or strong tone burst stimuli at 100 dB sound
132 pressure level (SPL) (Figure 2A-B). As reported previously for *Cib2*$^{KO/KO}$ mice, we observed
133 that auditory hair cells in *Cib2*$^{KO/KO}$*;Cib3*$^{KO/KO}$ mice did not accumulate FM 1-43 dye (Figure
134 2C). Also, similar to *Cib2*$^{KO/KO}$ mice (Giese et al., 2017; Michel et al., 2017; Wang et al., 2017),
135 we observed progressive degeneration of auditory hair cells in *Cib2*$^{KO/KO}$*;Cib3*$^{KO/KO}$ mice
136 (Figure 2D). Taken together with previous studies, our results confirm that CIB2 is
137 indispensable for hearing and MET function in the auditory hair cells. Furthermore,
138 endogenous CIB3 is unable to compensate for CIB2 loss in the auditory hair cells, perhaps due
139 to extremely low expression level of CIB3 in these cells and the lack of compensatory
140 overexpression of CIB3 in the cochlea of *Cib2*$^{KO/KO}$ mice (Giese et al., 2017).

141

142 **CIB2 and CIB3 are required for vestibular function in mice**

143 After we assessed auditory function, we turned our analyses toward vestibular function.
144 Similar to *Cib2*$^{KO/KO}$ mice (Giese et al., 2017), *Cib3*$^{KO/KO}$ mice did not display any obvious

145 indications of vestibular dysfunction, such as circling, hyperactivity or head bobbing,
146 performed well when exploratory behavior was tested, and had normal vestibulo-ocular
147 reflexes (Figure 3). In contrast, visual observation of the *Cib2*$^{KO/KO}$;*Cib3*$^{KO/KO}$ mice indicated
148 altered exploratory behavior in an open-field test, suggesting an impairment of the vestibular
149 system (Figure 3A). To assess the implications of the *Cib2*$^{KO/KO}$;*Cib3*$^{KO/KO}$ mice on vestibular
150 function, we next performed a series of tests, including: the vestibulo-ocular reflex (VOR),
151 performance in a rotating rod, and head movement analysis (Figure 3B-H). The VOR is
152 mediated by a direct three neuron pathway linking the vestibular nerve to the extraocular
153 muscles and produces compensatory eye movements in the direction opposite of the head
154 movement to provide stable gaze (reviewed in Cullen, 2019). The dynamic response properties
155 (i.e., gain and phase) of the VOR can be precisely quantified in response to rotations applied
156 at different frequencies in darkness (VORd). In response to VORd testing, *Cib2*$^{+/+}$;*Cib3*$^{KO/KO}$
157 mice generated robust compensatory eye movements (Figure 3B, black trace). In contrast,
158 *Cib2*$^{KO/KO}$;*Cib3*$^{KO/KO}$ mice generated negligible eye movements (Figure 3B, red trace).
159 Consistent with this observation, quantification of the VORd across frequencies (Figure 3C)
160 revealed gains near zero in the *Cib2*$^{KO/KO}$;*Cib3*$^{KO/KO}$ mice that were significantly reduced
161 ($p<0.05$) compared to those measured in *Cib2*$^{+/+}$;*Cib3*$^{KO/KO}$ mice. Interestingly, the VORd
162 gains of *Cib2*$^{KO/+}$;*Cib3*$^{KO/KO}$ mice also showed attenuation with a significant decrease at 2 Hz
163 ($p<0.01$) compared to *Cib2*$^{+/+}$;*Cib3*$^{KO/KO}$ mice. On the other hand, the response phase of VORd
164 eye movements were comparable for *Cib2*$^{KO/+}$;*Cib3*$^{KO/KO}$ and *Cib2*$^{+/+}$; *Cib3*$^{KO/KO}$ mice at all
165 frequencies ($p>0.05$) (Figure 3C).

166 As a control for possible changes in visual system and/or ocular motor pathway, we
167 also quantified the optokinetic reflex (OKR), which generates eye movements in responses to
168 a moving visual scene and in light. The OKR normally works together with the VOR to

169 stabilize the visual field on the retina. Both *Cib2*$^{+/+}$;*Cib3*$^{KO/KO}$ and *Cib2*$^{KO/+}$;*Cib3*$^{KO/KO}$ showed
170 robust OKN responses which similarly decreased as a function of frequency (Figure 3D;
171 $p>0.05$). Likewise, OKR gain values in *Cib2*$^{KO/KO}$;*Cib3*$^{KO/KO}$ were comparable with the single
172 exception of a significant gain decrease at 0.2 Hz ($p<0.05$). Analysis of OKN similarly revealed
173 comparable response phase for all 3 groups of mice at all frequencies ($p>0.05$) with the
174 exception that the *Cib2*$^{KO/KO}$;*Cib3*$^{KO/KO}$ mice demonstrated less lag at 0.8 and 2 Hz (Figure 3D-
175 E). Overall, the OKR responses of mutant and control mice were generally comparable.

176 In addition to generating compensatory VOR eye movements to stabilize gaze, the
177 vestibular system also plays a key role in the maintenance of posture and control of balance.
178 Thus, we also tested all 3 groups of mice on several vestibular tasks that assessed balance and
179 postural defects. First, quantification of open-field testing experiments confirmed that mice
180 exhibited circling – a behavior that is commonly associated with loss of vestibular function in
181 mice (Figure 3F; $p<0.002$). We also completed rotarod testing in which performance was
182 quantified by measuring the amount of time the mouse remained on the rotating rod as its
183 acceleration increased. While *Cib2*$^{+/+}$;*Cib3*$^{KO/KO}$ and *Cib2*$^{KO/+}$;*Cib3*$^{KO/KO}$ mice exhibited
184 similar performance, *Cib2*$^{KO/KO}$;*Cib3*$^{KO/KO}$ mice exhibited significantly poorer performance
185 across all time points from day 1 through day 4 (Figure 3G, $p<0.002$). Finally, it was also
186 possible to distinguish *Cib2*$^{KO/KO}$;*Cib3*$^{KO/KO}$ mice from the other two groups in their home
187 cages since they commonly displayed head bobbing, a trait also generally associated with
188 vestibular dysfunction in mice. To quantify head movement in our mice, we attached a 6D
189 MEMS module consisting of three gyroscopes and three linear accelerometers to the mouse's
190 head implant (see Methods). Analysis of power spectra of head motion revealed significantly
191 higher power for *Cib2*$^{KO/KO}$;*Cib3*$^{KO/KO}$ mice in all six dimensions of motion, as compared to
192 *Cib2*$^{KO/+}$;*Cib3*$^{KO/KO}$ and *Cib2*$^{+/+}$;*Cib3*$^{KO/KO}$ mice (Figure 3H, compare red vs. blue and black).

193 Further, there were no significant differences in the head movements power spectra of
194 *Cib2*$^{KO/+}$;*Cib3*$^{KO/KO}$ and *Cib2*$^{+/+}$;*Cib3*$^{KO/KO}$ mice (Figure 3H**,** blue vs. black). Taken together
195 our findings indicate that *Cib2*$^{KO/KO}$;*Cib3*$^{KO/KO}$ mice show marked deficits in vestibulomotor
196 function when compared to both *Cib2*$^{KO/+}$;*Cib3*$^{KO/KO}$ and *Cib2*$^{+/+}$;*Cib3*$^{KO/KO}$ mice.

197

198 **CIB2 and CIB3 are functional subunits of the MET apparatus in mouse vestibular hair**
199 **cells**

200 To understand the root cause of vestibulomotor function deficits described above for
201 *Cib2*$^{KO/KO}$;*Cib3*$^{KO/KO}$ mice, we first analyzed vestibular hair bundle morphology using confocal
202 microscopy. High-resolution confocal imaging did not reveal any obvious vestibular hair cell
203 loss and hair bundles looked indistinguishable from control in *Cib2*$^{KO/KO}$;*Cib3*$^{KO/KO}$ mice
204 (Figure 4A). Next, we visualized MET activity in vestibular hair cells of saccular and utricular
205 end organs of *Cib2*$^{KO/KO}$;*Cib3*$^{KO/KO}$ mice using the styryl dye FM 1-43. These vestibular end
206 organs are divided into two main physically and functionally distinct domains, a central striolar
207 domain and a peripheral extrastriolar domain. At P5, FM 1-43 labeling of *Cib2*$^{KO/KO}$; *Cib3*$^{KO/KO}$
208 tissue failed to label vestibular hair cells in appreciable numbers (Figure 4B). Similarly, fixable
209 FM 1-43FX intraperitoneal injections at P60 also showed no dye uptake in *Cib2*$^{KO/KO}$;
210 *Cib3*$^{KO/KO}$ mice (Figure 4C). *Cib2*$^{KO/KO}$ and *Cib3*$^{KO/KO}$ single mutant mice had dye uptake both
211 in striolar and extrastriolar hair cells, although a subtle reduction in FM 1-43FX was observed
212 in extrastriolar hair cells of both single mutants at P60 (Figure 4C). Taken together, these
213 results indicate that CIB2 and CIB3 have functionally redundant but compulsory roles in the
214 vestibular hair cell MET complex.

215

216 **Cib2 and Cib3 function is evolutionary conserved in zebrafish**

217 Numerous studies have shown that the same proteins are required for hair cell MET in
218 zebrafish and mammals (Chen et al., 2020; Erickson et al., 2017; Ernest et al., 2000; Gleason
219 et al., 2009; Gopal et al., 2015; Maeda et al., 2017, 2014; Phillips et al., 2011; Seiler et al.,
220 2004; Söllner et al., 2004). Unlike mammals, the zebrafish inner ear does not have a cochlea.
221 Instead, zebrafish rely on their saccule for hearing and utricle for balance. Zebrafish also utilize
222 hair cells in a specialized sensory system, the lateral line, to detect local water movement. The
223 hair cells within both the zebrafish inner ear and lateral line share many morphologically
224 similarities to mammalian vestibular hair cells (Nicolson, 2017). Given the zebrafish reliance
225 on the saccule for hearing and the similarities between zebrafish hair cells to mammalian
226 vestibular hair cells, we tested whether Cib2 and/or Cib3 were required for hair cell MET in
227 the zebrafish inner ear or lateral line.

228 To examine the impact of Cib2 and Cib3 loss in zebrafish, we created mutants using
229 CRISPR-Cas9 based methods to target each homologue (Varshney et al., 2016). We first
230 examined auditory function by testing the acoustic startle reflex in *cib2* and *cib3* mutants. For
231 our experiments we used a Zantiks behavioral system to quantify the probability of generating
232 a startle in response to a vibrational tap stimulus. This response is thought to rely primarily on
233 hair cells in the zebrafish inner ear and lateral-line system. We found that, compared to
234 controls, the probability of a startle response was significantly reduced in *cib2* mutants (Figure
235 5A, control: 0.71 ± 0.04; *cib2*: 0.28 ± 0.06, $p = 0.005$). In contrast, *cib3* mutants startle with a
236 similar frequency compared to controls (Figure 5A, $p = 0.36$). Interestingly, contrary to
237 mammals, where CIB2 is crucial for hearing, acoustic startle responses were not completely
238 eliminated in *cib2* mutants. One possibility for this partial loss of acoustic startle is that Cib3
239 may be able to compensate for Cib2 in the zebrafish. Therefore, we examined acoustic startle
240 responses in *cib2;cib3* mutants. In *cib2;cib3* mutant animals we observed a complete absence
241 of startle responses (Figure 5A). Furthermore, we observed that *cib2;cib3* mutants but not *cib2*

242 or *cib3* mutants exhibited spontaneous circling behavior, an additional indicator of inner ear
243 dysfunction in zebrafish (Nicolson et al., 1998). Together our behavioral results indicate that
244 Cib2 and Cib3 are both required to ensure normal acoustic startle responses in zebrafish.
245 Furthermore, just loss of Cib2, but not Cib3 can impair auditory function in zebrafish.
246
247 **Cib2 and Cib3 are required for MET in the zebrafish lateral line**
248 Our results demonstrate that both Cib2 and Cib3 are required for proper auditory
249 function in zebrafish. This raises the question of whether, similar to mice, these proteins are
250 critical for MET function in zebrafish hair cells. Therefore, we next turned our analysis to hair
251 cells in neuromast organs of the lateral line where methods to assess MET are well-documented
252 and straightforward (Lukasz and Kindt, 2018; Seiler et al., 2004).
253 First, to assess whether there were gross alterations to MET in lateral-line hair cells we
254 examined uptake of the FM 1-43. We found that, compared to controls, the percent of hair cells
255 per neuromast labeling with FM 1-43 was significantly reduced in *cib2* mutants (Figure
256 5B,D,E, control: 97.60 ± 1.17; *cib2*: 37.53 ± 6.92, $p < 0.0001$). In contrast, a similar percent of
257 hair cells per neuromast labeled with FM 1-43 in *cib3* mutants, compared to controls (Figure
258 5B,D,F, *cib3*: 95.67 ± 1.87, $p = 0.97$). We also quantified the average intensity of the FM 1-43
259 in hair cells (Figure 5C). We found that, compared to controls, the average FM 1-43 label was
260 reduced in *cib2* but not *cib3* mutants (Figure 5C). The residual FM 1-43 label in *cib2* mutant
261 hair cells led us to hypothesize that in lateral-line hair cells, similar to its role in zebrafish
262 auditory function, Cib3 may be able to substitute for Cib2 in MET. To assess whether Cib3
263 can substitute for Cib2, we examined FM 1-43 labeling in *cib2;cib3* mutants. In *cib2;cib3*
264 mutant animals we observed a complete absence of FM 1-43 labeling in lateral-line hair cells
265 (Figure 5B,D,G). Thus, taken together the results of our FM 1-43 labeling analysis are

266 consistent with a requirement for both Cib2 and Cib3 in hair cell MET in the zebrafish lateral
267 line.

268 To obtain a more quantitative assessment of MET we used Ca^{2+} imaging to perform
269 evoked measurements of hair cell function. For this assessment, we used a transgenic line that
270 expresses a membrane-localized GCaMP6s (memGCaMP6s) specifically in hair cells (Figure
271 5H-I'). This transgenic line has previously been used to measure Ca^{2+} influx into apical hair
272 bundles while stimulating lateral-line hair cells with a fluid-jet (Figure 5H-I') (Lukasz and
273 Kindt, 2018). Using this approach, we were able to stimulate and monitor stimulus-evoked
274 mechanosensitive Ca^{2+} responses in hair bundles within neuromast organs of each genotype
275 (Representative responses: Figure 5I-L). We quantified the number of hair bundles per
276 neuromast with mechanosensitive Ca^{2+} responses, and found that compared to controls,
277 significantly few hair bundles were mechanosensitive in *cib2* and *cib2*;*cib3* mutants (Figure 5-
278 figure supplement 1A, control: 92.16 ± 2.49; *cib2*: 49.88 ± 5.79, *cib2;cib3:* 18.99 ± 6.63, $p >$
279 0.0001). In contrast, in *cib3* mutants, the percent of mechanosensitive hair bundles per
280 neuromast was similar compared to controls (Figure 5-figure supplement 1A, *cib3*: 94.51 ±
281 1.82, $p = 0.96$). We also quantified the magnitude of the mechanosensitive Ca^{2+} signal in the
282 hair bundles, focusing on only the responsive hair cells for each genotype. This quantification
283 revealed that, while *cib3* mechanosensitive responses were not different compared to controls
284 (Figure 5-figure supplement 1B-C, GCaMP6s % $\Delta F/F$ control: 70.60 ± 5.87; *cib3*: 71.61 ±
285 5.23, $p > 0.998$), the magnitude of responses in *cib2* and *cib2*;*cib3* hair bundles was
286 significantly reduced (Figure 5-figure supplement 1B-C, GCaMP6s % $\Delta F/F$ control: 70.60 ±
287 5.87; *cib2*: 32.95 ± 5.77, *cib2;cib3:* 14.65 ± 1.85, $p < 0.0001$). Overall, our *in vivo* FM 1-43
288 and Ca^{2+}-imaging analyses revealed that Cib2 and Cib3 are both required to ensure normal
289 MET function in lateral-line hair cells. Furthermore, loss of Cib2 alone, but not Cib3 can impair
290 mechanosensory function in zebrafish lateral-line hair cells.

291

292 **Cib2 is required in specific subsets of hair cells in the zebrafish lateral line and inner ear**

293 Previous work has shown that within the zebrafish inner ear and lateral line there are
294 distinct hair cell subtypes that rely on different complements of the mechanosensitive ion
295 channel Tmc: Tmc1, 2a and 2b. In the primary posterior lateral line (pLL) hair cells are oriented
296 to respond to either anterior or posterior fluid flow. The subset of hair cells that detects posterior
297 flow relies on Tmc2b while the subset that detects anterior flow relies on both Tmc2b and
298 Tmc2a (Figure 6A) (Chou et al., 2017). Further, in the zebrafish inner ear, work has shown that
299 there are two morphologically distinct types of hair cells: short, teardrop-shaped cells with
300 taller hair bundles and tall, gourd-shaped cells with shorter hair bundles (Smith et al., 2020;
301 Zhu et al., 2021). Short cells rely on Tmc2a, while tall cells rely on either Tmc1 or Tmc2b for
302 mechanosensitive function (Figure 6E). Based on this work, we hypothesized that Cib2 or Cib3
303 could have specific roles in zebrafish hair cell sensory organs linked to hair cell orientation in
304 the lateral line or morphology type in the inner ear.

305 Our FM 1-43 labeling in neuromasts revealed no defect in *cib3* mutants, suggesting that
306 Cib2 can compensate for Cib3 in all pLL hair cells. In contrast to *cib3* mutants, only a subset
307 of hair cells per neuromast were labeled with FM 1-43 in *cib2* mutants (Figure 5E). Previous
308 work has shown that in the pLL of *tmc2b* mutants, a subset of hair cells that respond to anterior
309 flow label with FM 1-43 (Chou et al., 2017). This residual FM 1-43 label is dependent on
310 Tmc2a. Therefore, we examined whether the remaining, FM 1-43 positive hair cells in *cib2*
311 mutants have a specific hair cell orientation. For this analysis, we used a fixable form of FM
312 1-43, FM 1-43FX to label hair cells. After FM 1-43FX labeling, we fixed the larvae and labeled
313 the apical hair bundles with phalloidin to reveal hair cell orientation. This analysis revealed
314 that in sibling controls, a similar percentage of FM 1-43FX positive hair cells are oriented to
315 respond to anterior and posterior flow (Figure 6B,B',D). In contrast, when we examined *cib2*

316 mutants, we found that significantly more of the FM 1-43 positive hair cells were oriented to
317 respond to posterior flow (Figure 6C-D). This indicates that in *cib2* mutants, the residual Cib3
318 present in pLL hair cells preferentially functions in hair cells that express primarily Tmc2b and
319 are oriented to respond to posterior flow (Figure 6A). On the other hand, Cib2 can function
320 with hair cells that express Tmc2b (respond to posterior flow) as well as hair cells that express
321 Tmc2b and Tmc2a (respond to anterior flow).

322 Next, we examined whether different hair-cell subtypes (short versus tall morphology)
323 in the zebrafish inner ear preferentially rely on Cib2 or Cib3 for mechanosensitive function.
324 To examine MET function, we injected FM 4-64 into the zebrafish ear in a transgenic
325 background that labels the hair cell membrane (memGCaMP6s). FM 4-64 is a redshifted
326 version of FM 1-43 and provides a similar readout of MET (Erickson et al., 2017; Smith et al.,
327 2020). After injection, we imaged FM 4-64 label in the medial cristae, an inner ear sensory
328 organ that allows for excellent delineation of short and tall cell types (Figure 6F-F'). We found
329 that similar to our FM 1-43 results in the pLL, no hair cells in the medial cristae were FM 4-
330 64 positive in *cib2;cib3* double mutants (Figure 6I-I'). In addition, similar to the pLL we
331 observed no defects in FM 4-64 labeling in the crista of *cib3* mutants compared to controls
332 (Figure 6G-G'). Interestingly we found that short hair cells in the crista of *cib2* mutants failed
333 to label with FM 4-64 (Figure 6H-H'). Previous work has shown that short hair cells rely on
334 Tmc2a for mechanosensitive function (Smith et al., 2020). Overall, our functional assessment
335 of MET based on hair cell subtypes within the zebrafish pLL and inner ear suggests that Cib2
336 is required for mechanosensitive function in hair cells that express Tmc2a.

337

338 **CIB proteins simultaneously interact with at least two cytoplasmic domains of TMC1**

339 To gain molecular insight into the role played by CIB proteins in hair-cell MET, we
340 generated AlphaFold 2 (AF2) (Jumper et al., 2021; Tunyasuvunakool et al., 2021) models of

341 the human TMC1 dimer, alone and in complex with human CIB2/3 (Figure 7A-B; Figure 7-
342 figure supplement 1; Figure 7-video 1). The AF2 model of TMC1 alone resembles previous
343 TMEM16/OSCA-based models of TMC1 and is also consistent with a recent cryo-EM
344 structure of the worm TMC-1 protein (Ballesteros et al., 2018; Jeong et al., 2022; Pan et al.,
345 2018; Walujkar et al., 2021). In these models, TMC1 has ten transmembrane domains (α1 to
346 α10; Figure 7-figure supplements 1-2) and a putative pore is formed by transmembrane helices
347 α4, α5, α6, and α7 at the periphery of each monomer (Pan et al., 2018; Walujkar et al., 2021),
348 away from the dimeric interface involving α10. Our new models feature an additional
349 amphipathic helix, which we denote α0, extending almost parallel to the expected plane of the
350 membrane bilayer without crossing towards the extracellular side (as observed for a mostly
351 hydrophobic α0 in OSCA channels) (Jojoa-Cruz et al., 2018; Liu et al., 2018; M. Zhang et al.,
352 2018). Extracellular and intracellular domains linking transmembrane helices, which were
353 either omitted or poorly predicted in previous work (Ballesteros et al., 2018; Pan et al., 2018;
354 Walujkar et al., 2021), have well-defined secondary structure and a high confidence score
355 (pLDDT > 70 for most regions; Figure 7-figure supplement 1A). The intracellular domain
356 linking helices α2 and α3, denoted here as IL1, adopts a helix-loop-helix with the two helices
357 running parallel to each other and differing in length. This is the same fold observed in its
358 crystal structure in complex with CIB3 (Figure 7-figure supplements 1-5) (Liang et al., 2021),
359 which validated the modeling approach.

360 Interestingly, AF2 models of TMC1 in complex with CIB2 suggest that the N-terminus
361 (NT) of TMC1 also interacts with CIB2 (Figure 7A-B). In our model, CIB2 is clamped between
362 TMC1-NT and TMC1-IL1 while the first helix of TMC1-IL1 runs parallel to the membrane
363 plane interacting with the base of α1 and the intracellular linkers between α4 and α5, α6 and
364 α7, and α8 and α9. Notably, the predicted interaction between TMC1-NT and CIB2 is

365 consistent with previous biochemical data (Giese et al., 2017), while the overall model resolves
366 seemingly contradictory results indicating that either the NT or IL1 of TMC1 were responsible
367 for interactions with CIB proteins (Giese et al., 2017; Liang et al., 2021). Additional AF2
368 models of TMC1 with CIB3 and of TMC2 with CIB2/3 (Figure 7-figure supplement 1)
369 predicted the same architecture for the TMC1/2 + CIB2/3 complexes where CIB proteins are
370 clamped between the IL1 and NT domains of TMCs. Predictions for fish complexes also show
371 the same general architecture (Figure 7-figure supplement 1A).

372 Nuclear magnetic resonance (NMR) experiments were used to validate the clamp
373 model for *Homo sapiens* (*hs*) TMC + CIB interactions. We produced uniformly ^{15}N labeled *hs*
374 CIB2 (22.7 kDa) and CIB3 (22.9 kDa) proteins ([U-^{15}N]-*hs* CIB2/3), alone or co-refolded with
375 unlabeled *hs* TMC1-IL1 (6.3 kDa). In parallel, we produced an unlabeled soluble TMC1-NT
376 fragment (6.9 kDa) and used these CIB and TMC1 samples to test protein-protein interactions
377 by monitoring their effects on 2D ^{1}H-^{15}N-correlation spectra of the labeled CIB2 and CIB3
378 proteins. All protein fragments were purified using size exclusion chromatography (SEC)
379 (Figure 7-figure supplement 6), revealing a single monodisperse peak for [U-^{15}N]-*hs* CIB2
380 (69.2 mL elution volume in S75 16/600 column) and a slightly displaced peak for [U-^{15}N]-*hs*
381 CIB2 + *hs* TMC1-IL1 (68.5 mL). In contrast, SEC experiments revealed two peaks for [U-
382 ^{15}N]-*hs* CIB3 alone (potential dimer at 62.8 mL and potential monomer at 73.1 mL) and a
383 single peak for [U-^{15}N]-*hs* CIB3 + *hs* TMC1-IL1 (71.3 mL). ^{1}H-^{15}N-correlation spectra of [U-
384 ^{15}N]-*hs* CIB2 alone were consistent with prior data indicating that many, but not all potential
385 peaks are resolved (Figure 7C, Figure 7-figure supplement 7A) (Huang et al., 2012). Spectra
386 for the [U-^{15}N]-*hs* CIB2 + *hs* TMC1-IL1 complex exhibit widespread perturbations, consistent
387 with extensive remodeling of the CIB2 structure. Moreover, addition of *hs* TMC1-NT induced
388 additional chemical shift perturbations in many, but not all peaks, demonstrating that the
389 TMC1-IL1 and TMC1-NT ligands bind simultaneously to [U-^{15}N]-*hs* CIB2 (Figure 7C, Figure

390 7-figure supplement 7B). We observed similar results when comparing spectra for [U-^{15}N]-*hs*
391 CIB3 alone, co-refolded with *hs* TMC1-IL1, and upon addition of *hs* TMC1-NT (Figure 7-
392 figure supplement 7C-D). A control experiment with the co-refolded mix of *hs* CIB3 + *hs*
393 TMC1-IL1 and [U-^{15}N]-*hs* CIB2 (Figure 7-figure supplement 7E) revealed no change in
394 chemical shifts indicating that direct heteromeric interactions between CIB2 and CIB3 are
395 unlikely. Thus, taken together, the NMR data strongly support a model in which human CIB2/3
396 proteins are clamped between TMC1-IL1 and TMC1-NT as suggested by AF2 and consistent
397 with prior biochemical data revealing interactions with either TMC1-NT or TMC1-IL1 (Giese
398 et al., 2017; Liang et al., 2021).
399
400 **Simulations reveal CIB proteins stabilize TMC1 and TMC2**
401 Our dimeric AF2 models of TMC1/2 alone and in complex with CIB2/3 are consistent
402 with previous experimental data that validated the location of the putative pore in similar
403 TMEM16/OSCA-based homology models of TMC1 (Pan et al., 2018). Our models are also
404 consistent with our NMR data supporting the clamp model for the TMC + CIB complex (Figure
405 7C). To improve the AF2 predictions and to gain mechanistic insights into TMC and CIB
406 function we turned to all-atom equilibrium molecular dynamics (MD) simulations (Karplus
407 and Petsko, 1990). We built ten different models that included dimeric TMC1 or TMC2 alone,
408 in complex with CIB2 or CIB3 with and without bound Ca^{2+}. These models were embedded in
409 either pure POPC or stereocilia-like mixed composition bilayers and solvated to generate a
410 total of twenty systems that were equilibrated for 100 ns each (Figure 7D, Figure 7-Table
411 supplement 1).
412 Equilibrium simulations of TMC1 and TMC2 alone revealed stable conformations for
413 the transmembrane domains of these proteins, but a highly mobile NT domain (Figure 7E,
414 Figure7-figure supplement 8). In simulations where CIB2 or CIB3 were present, with or

415 without bound Ca^{2+}, we observed more stable conformations of N-termini along with stable
416 salt bridges (Figure 7F). Buried surface area (BSA) for the TMC + CIB complexes (Figure 7-
417 figure supplement 9A,C,E, Table supplement 2) revealed a possible trend in which TMC1 and
418 TMC2 have more contacts with CIB3 than with CIB2. While additional sampling and longer
419 simulations might be needed for a robust prediction, these results suggest variable affinities for
420 TMC + CIB protein complexes that might be modulated by Ca^{2+} (Figure 7-figure supplement
421 9F).

422 Additional analysis of the putative pore in our simulations of TMC1 and TMC2
423 revealed hydration as observed in previous simulations of TMEM16/OSCA-based TMC1
424 models, as well as movement of lipids that lined up the predicted permeation pathway for
425 cations suggesting a membrane-based gating mechanism (Pan et al., 2018; Sukharev and
426 Corey, 2004; Walujkar et al., 2021). Longer, Anton 2, 960-ns long equilibrium trajectories of
427 TMC1 with CIB2 and bound Ca^{2+} in a mixed bilayer and TMC1 with CIB2 and (un)bound
428 Ca^{2+} in a POPC bilayer revealed how parts of the amphipathic α0 helices spontaneously
429 partitioned at the membrane interface with their hydrophobic sides pointing toward the lipid
430 bilayer core (Figure 7G). The N-terminal cytoplasmic domain of LHFPL5 has been shown to
431 interact with this TMC1 amphipathic helix, which might be essential for channel function in
432 mice (Qiu et al., 2023). The BSA for the dimeric TMC1 + CIB2 complex in these longer
433 simulations (Figure 7-figure supplement 9E) decreased as contacts between TMC1-α0 and
434 CIB2 were lost for one of the monomers in the mixed bilayer system. In the monomer in which
435 contacts were maintained, a single cholesterol was situated in the middle of the putative pore.
436 Similarly, TMC1-α0 and CIB2 contacts were lost for both monomers in the POPC bilayer
437 systems. Regardless, in all Anton 2 equilibrium trajectories contacts between CIB2 and the

438 TMC1-IL1 and -NT remained, thus confirming the stability of the complex over a microsecond
439 timescale.
440
441 **TMC1 and TMC2 complexes with CIB2 and CIB3 are predicted to be cation channels**
442 To further explore the properties of our models of TMC/CIB complexes we took
443 equilibrated TMC1 systems and applied a -0.5 V transmembrane voltage while monitoring ion
444 permeation through the putative pore during 100-ns long trajectories (Figure 7-figure
445 supplements 10-11, Figure 7-Table supplement 2, Figure 7-video 2). In systems with pure
446 POPC bilayers we observed permeation of K^+ in either one or both pores of the TMC1 dimer,
447 with or without CIB2 or CIB3 and with or without bound Ca^{2+}. Similar results were obtained
448 for four TMC1 systems simulated at -0.25 V. Variability of the conductance state was attributed
449 to partial blockage by lipids and poor sampling, but in all cases in which a clear conductive
450 state was monitored we observed almost exclusive passage of K^+ with conductance values that
451 reached up to ~138 pS for a single pore. While simulations tend to overestimate bulk KCl
452 conductivity and in some cases predictions need to be scaled down (by a factor of ~0.6)
453 (Walujkar et al., 2021), the conductance values monitored here are consistent with previous
454 simulations and with the expected conductance of the inner-ear transduction channel (Beurg et
455 al., 2021; Walujkar et al., 2021). In contrast, we observed smaller conductance values for
456 TMC1 systems with mixed lipid bilayers (at most ~22 pS for a single pore), regardless of the
457 presence of CIB2 or CIB3, with or without bound Ca^{2+} (Figure 7-figure supplement 11B).
458 Additional Anton 2 simulations for one of these TMC1 + CIB2 + Ca^{2+} systems with a mixed
459 membrane, equilibrated for 240 ns and then subjected to -0.43 V for 480 ns, revealed a low
460 conductance value of ~6.2 pS. The reduced conductance values observed for mixed-membrane
461 systems were attributed in part to pore blockage by cholesterol and lipids in the initial setup.
462 Interestingly, Anton 2 simulations of TMC1, TMC1 + CIB2, and TMC1 + CIB2 + Ca^{2+} in pure

463 POPC membranes subjected to -0.5 V, -0.25 V, and -0.125 V for 480 ns, 480 ns, and 960 ns,
464 respectively, revealed a trend in which TMC1 exhibits higher conductance with CIB2 bound
465 (Figure 7H, Table supplement 2). This may begin to explain why CIB2 is essential for normal
466 TMC1 function.

467 Simulations of TMC2 with an applied transmembrane voltage of -0.5 V revealed a more
468 closed state when compared to our TMC1 model, regardless of membrane composition and
469 presence or absence of CIB2, CIB3 and bound Ca^{2+} (Figure 7-figure supplement 11).
470 Conduction of K^+ was observed in most cases, but the maximum conductance did not reach
471 above ~42 pS, suggesting that the conformation simulated is less open than the ones explored
472 in simulations of TMC1. Regardless, our simulations unequivocally indicate that TMC1 and
473 TMC2 are cation channels and that these proteins can form stable complexes with CIB2 and
474 CIB3.

475

476 **Discussion**

477 Previous work on CIB proteins had primarily focused on mammalian auditory hair
478 cells, leaving open the question of whether they play a functional role in vestibular function
479 and across vertebrate species. Recently, Wang et al. have suggested that CIB2 and CIB3 are
480 important for stereocilia maintenance and MET in mouse vestibular hair cells (Wang et al.,
481 2023). This work demonstrated that similar to *Tmc1* and *Tmc2*, *Cib2* is highly expressed in the
482 striolar region while *Cib3* is expressed in the extrastriolar regions, and mice lacking both *Cib2*
483 and *Cib3* had no MET and deficits in vestibular hair cell bundle structure (Wang et al., 2023).
484 Taking a step forward, here, we now establish that CIB2 and CIB3 are highly conserved
485 regulators of MET in both mouse vestibular hair cells and zebrafish hair cells. We demonstrate
486 that vestibular hair cells in mice and zebrafish lacking CIB2 and CIB3 appear structurally

487 normal but have no detectable MET, assessed via FM 1-43 dye uptake, at time points when
488 MET function is well developed in wild-type hair cells. Similar structural-function phenotype
489 has been reported in auditory hair cells in *Tmc1/Tmc2* double mutant mice (Kawashima et al.,
490 2015). Besides the known *in vitro* interactions (Giese et al., 2017; Liang et al., 2021), our study
491 provides strong genetic evidence for the direct functional relationship between CIB and TMC
492 proteins in regulating MET both in auditory and vestibular hair cells.

493 Previous studies have shown that the loss of CIB2 leads to profound hearing loss from
494 birth in both human and mice (Giese et al., 2017; Liang et al., 2021; Seco et al., 2016). This
495 suggests that the endogenous levels of CIB3 present in auditory hair cells are not sufficient to
496 compensate for CIB2 in hearing. Prior work has also shown that over-expression of CIB3 in
497 mouse auditory outer hair cells can only partially compensate for the loss of CIB2 in MET
498 (Liang et al., 2021). However, whether overexpression of CIB3 can rescue impaired hearing
499 thresholds in *Cib2* mutant mice is not known. While CIB2 is also present in vestibular hair
500 cells, compared to auditory hair cells, the expression of CIB3 is several folds higher in
501 vestibular end organs. Indeed, our current data demonstrate that, unlike auditory hair cells,
502 endogenous levels of CIB3 can fully compensate for loss of CIB2 in vestibular hair cells in
503 mice. Together our work on the vestibular system in mice highlights that both CIB2 and CIB3
504 can play overlapping roles in MET function.

505 Interestingly, our corresponding work in zebrafish indicates that Cib3 can also
506 compensate for Cib2, but only in specific subsets of hair cells. Recent genetic, morphology and
507 scRNAseq data have revealed that within the zebrafish inner ear, each sensory epithelia
508 (utricle, saccule, cristae) have two distinct types of hair cells (Shi et al., 2023; Smith et al.,
509 2020). In these epithelia, short cells are present in the striolar or central region, while tall cells
510 are present in the extrastriolar or peripheral region (Figure 6A,E). Genetic studies have

511 revealed that these two types of hair cells rely on different Tmc combinations for MET–short
512 cells rely on Tmc2a while tall cells rely on Tmc2b and Tmc1 (Smith et al., 2020). Recent
513 scRNAseq work has validated this *Tmc* requirement and shown that *cib2* is expressed in both
514 short and tall cells, while *cib3* is specifically expressed in just tall cells (Shi et al., 2023). Our
515 work on MET in the zebrafish inner ear provides functional support for this *cib* RNAseq data,
516 as FM 4-64 labeling is absent from short hair cells when Cib2 is lost (Figure 6H). In contrast,
517 loss of Cib3 alone does not impact FM 4-64 labeling in the zebrafish inner ear, indicating that
518 Cib2 can compensate for loss of Cib3 in both short and tall cells (Figure 6G). Currently it is
519 not clear what role these two distinct types of hair cells play in zebrafish hearing and balance.
520 Behavioral work on zebrafish *tmc2a* mutants has shown that when MET is absent from just
521 short hair cells, the acoustic startle response is severely diminished (Smith et al., 2020). This
522 is consistent with our present findings showing that zebrafish *cib2* mutants with impaired MET
523 in short hair cells have a reduced acoustic startle response (Figure 5A). Together these
524 behavioral studies suggest that short hair cells play an important role in detecting acoustic
525 stimuli necessary to generate a robust escape behavior.

526 In addition to the inner ear, we likewise found that both Cib2 and Cib3 play an
527 important role in the zebrafish lateral line. Similar to the zebrafish inner ear and mouse
528 vestibular system, we show that in lateral-line hair cells, Cib2 can compensate for MET in all
529 hair cells when Cib3 is lost (Figure 5B,C,F,K, Figure 5-figure supplement 1A-C). However,
530 like in the zebrafish inner ear, when Cib2 is lost, MET is lost from a specific population of
531 lateral-line hair cells. In the lateral line, each neuromast has two cell populations that detect
532 flow in opposing directions (López-Schier and Hudspeth, 2006; Pujol-Martí and López-Schier,
533 2013). Work in the posterior lateral line has demonstrated that cells that detect anterior flow
534 rely on Tmc2a/2b for MET, while cells that detect posterior flow rely on just Tmc2b (Chou et

535 al., 2017). In our work we find that cells that detect anterior flow primarily rely on Cib2 for
536 MET (Figure 6C-D). Further, this work indicates that Cib3 cannot compensate for loss of Cib2
537 in these cells. Interestingly, our functional assessment in the zebrafish lateral line and inner ear
538 suggests that Cib2 is specifically required for mechanosensitive function in populations of hair
539 cells that express Tmc2a. Whether Cib3 is unable to pair with Tmc2a or is simply not expressed
540 along with Tmc2a remains an unanswered question. The significance of this pairing is also
541 unclear. Recent work has shown that the addition of Tmc2a to lateral line cells that detect
542 anterior flow significantly augments the mechanosensitive responses of these cells (Kindig et
543 al., 2023). Whether Cib2 is required along with Tmc2a for these augmented responses remains
544 unclear.

545 Our *in vivo* studies of mouse TMC + CIB and zebrafish Tmc + Cib complexes suggest
546 a conserved functional relationship between these two protein families across vertebrates.
547 Structural predictions using AF2 show conserved folds for human and zebrafish proteins, as
548 well as conserved architecture for their protein complexes. Predictions are consistent with
549 previous experimentally validated models for the TMC1 pore (Ballesteros et al., 2018; Pan et
550 al., 2018), with the structure of human CIB3 coupled to mouse TMC1-IL1 (Liang et al., 2021),
551 with the architecture of the nematode TMC-1 and CALM-1 complex (Jeong et al., 2022), and
552 with our NMR data validating the interaction between human TMC1 and CIB2/3 proteins.

553 Taken together, the modeling predictions, NMR experiments, and simulations
554 presented here provide a structural framework to interpret and understand seemingly
555 contradictory results. In a previous study (Giese et al., 2017), we showed that the N-termini of
556 TMC1 and TMC2 interact with CIB2, and subsequent work (Liang et al., 2021) presented
557 biochemical data validating the interaction between the TMC1-NT with CIB2. However, X-
558 ray crystallography data demonstrated that the main interaction between TMC1 and CIB3

559 involved IL1, leaving the role played by CIB2-TMC-NT interactions unaddressed (Liang et
560 al., 2021). Here we show using NMR that both TMC1-NT and TMC1-IL1 bind to CIB2 and
561 CIB3 non-competitively. These interactions are consistent with AF2 models for TMC + CIB
562 complexes where CIB proteins are clamped between TMC1-NT and IL1. Simulations of these
563 models indicate that these interactions are stable and last for microseconds, with some potential
564 preferential binding of TMC1 and TMC2 to CIB3 over CIB2 predicted from BSA calculations.

565 Interestingly, the behavior of CIB2 and CIB3 in solution (SEC experiments) is different
566 in the absence of TMC1-IL1. While CIB2 appears as a single peak, CIB3 shows two clear
567 peaks indicating the presence of monomeric and dimeric states, consistent with the crystal
568 structure of an apparent CIB3 dimer (Liang et al., 2021). In the presence of TMC1-IL1, the
569 CIB3 dimeric peak is absent, and the potentially monomeric peak is slightly shifted accounting
570 for the added TMC1-IL1, as observed for CIB2. This result suggests that CIB2, both in the
571 presence and in the absence of TMC1-IL1, is monomeric in solution (Figure 7-figure
572 supplement 6). This proposal is consistent with prior conclusions that CIB2 is a monomer (Dal
573 Cortivo et al., 2019), but is in disagreement with other reports indicating that CIB2 is a dimer
574 in solution (Vallone et al., 2018) and our own prior pull-down assays indicating that CIB2 co-
575 immunoprecipitated with differentially tagged CIB2 or CIB3 (Giese et al., 2017; Riazuddin et
576 al., 2012). Moreover, our NMR data indicates that TMC1-IL1 + CIB2 is unlikely to directly
577 interact with CIB3. The simplest explanation for these seemingly contradictory results comes
578 from the TMC1 and TMC2 dimeric states (Pan et al., 2018) and our modeling indicating that
579 each TMC monomer interacts with one CIB protein (Figure 7-figure supplement 12). Pull-
580 down assays might simply be reflecting the oligomeric state of TMC proteins. In such scenario,
581 and considering that TMC proteins have been suggested to form hetero-oligomers (Pan et al.,
582 2018), there are up to ten different combinations of TMC1/2 and CIB2/3 proteins (Figure 7-

583 figure supplement 12) that might have distinct properties. Such variety of complexes with
584 potentially different conductance values might explain tonotopic changes of conductance along
585 the cochlea, although other explanations exist, including a variable number of TMC proteins
586 around the tip link (Beurg et al., 2018) and the direct influence of membrane composition on
587 conductance (Effertz et al., 2017; Walujkar et al., 2021).

588 Our simulations in the presence of a biasing potential unequivocally demonstrate that
589 both TMC1 and TMC2, in the presence or the absence of CIB proteins, with or without bound
590 Ca^{2+}, and in two types of membranes, are cation channels with predicted single-channel
591 conductance values that can reach values that are consistent with those of the transduction
592 channel. Our models emphasize again the role played by the membrane in lining the pore of
593 TMC proteins (Pan et al., 2018; Walujkar et al., 2021), and also indicate that CIB proteins are
594 ideally positioned to connect various parts of cytosolic inter-helix linkers with the helices that
595 form the pore, specially α3 and α4, recently implicated in gating (Akyuz et al., 2022; Walujkar
596 et al., 2021). Last, our modeling also positions the myristoylated N-terminus of CIB2 and CIB3
597 close enough to the membrane bilayer, which might be yet another way to sense membrane
598 stretch and influence gating.

599 Overall, the biochemically supported atomic-resolution structural models and
600 simulations presented here along with our results obtained using animal models strongly
601 suggest that TMC1/2 proteins must function with CIB2/3 in normal hair-cell MET across
602 sensory organs, hair-cell types, and species. This is supported by structural data indicating
603 multiple contact points between TMC and CIB proteins, simulation data predicting that CIB
604 proteins stabilize TMC cytosolic domains and may enhance cation conduction, and *in vitro* and
605 *in vivo* functional data indicating that both TMC1/2 and CIB2/3 proteins are needed for hair-
606 cell MET.

607 **Materials and methods**

608 **Key resources table**

REAGENT or RESOURCE	SOURCE	IDENTIFIER
Antibodies		
Goat anti-Mouse IgG (H+L) Highly Cross-Adsorbed Secondary Antibody, Alexa Fluor 568	Thermo Fisher Scientific	Cat#A-11031; RRID: AB_144696
Goat anti-Mouse IgG (H+L) Secondary Antibody, Alexa Fluor 488	Thermo Fisher Scientific	A32723
Goat anti-Rabbit IgG (H+L) Highly Cross-Adsorbed Secondary Antibody, Alexa Fluor 488	Thermo Fisher Scientific	Cat#A-11034; RRID: AB_2576217
Goat anti-rabbit IgG (H+L) Secondary Antibody, Alexa Fluor 568	Thermo Fisher Scientific	A-11011
Mouse monoclonal anti-FLAG M2	Sigma-Aldrich	Cat#F3165; RRID: AB_259529
Mouse monoclonal anti-FLAG M2-HRP	Thermo Fisher Scientific	Cat#A8592; RRID: AB_439702
Mouse monoclonal anti-V5	Thermo Fisher Scientific	Cat# R960-25; RRID: AB_2556564
Mouse monoclonal anti-V5-HRP	Thermo Fisher Scientific	Cat#R961-25; RRID: AB_2556565
Mouse monoclonal GAPDH	Santa Cruz	sc-32233
Rabbit polyclonal anti-CIB3	Sigma	SAB2103524
Rabbit polyclonal anti-GFP	Invitrogen	A-11122
Rabbit polyclonal anti-GFP-HRP	Thermo Fisher Scientific	Cat#A10260; RRID: AB_2534022
Rabbit polyclonal anti-Myosin VIIa	Proteus Biosciences	#25-6790
Rabbit polyclonal anti-V5	Abcam	Cat#ab9116; RRID: AB_307024
Chemicals		
FM™ 1-43FX	Thermo Fisher Scientific	F35355
FM™ 1-43	Thermo Fisher Scientific	T3163
FM™ 4-64	Thermo Fisher Scientific	T13320
Alexa Fluor™ 488 Phalloidin	Thermo Fisher Scientific	A12379
Alexa Fluor™ 633 Phalloidin	Thermo Fisher Scientific	A22284
16% Paraformaldehyde	Electron Microscopy Sciences	50-980-487

Triton X-100	Polysciences	04605-250
DAPI (4',6-Diamidino-2-Phenylindole, Dihydrochloride)	Invitrogen	D1306
Protease inhibitor mixture	Roche	11697498001
Protein A–Sepharose CL-4	Thermo Fisher Scientific	101042
Polyethylenimine	Polysciences	23966
Critical Commercial Assays		
4–20% Tris-Glycine gel	Novex	XV04205PK20
SMARTScribe Reverse Transcriptase kit	Clontech	639537
SYBRgreen technology	Qiagen	330503
Amersham™ ECL™ Prime Western Blotting Detection Reagent	GE Healthcare	RPN2236
QIAshredder	Qiagen	Cat#79656
Trans-Blot® Turbo™ Transfer System	Bio-Rad	Cat#1704156
Trans-Blot® Turbo™ Midi PVDF Transfer Packs	Bio-Rad	Cat#1704157
4–20% Mini-PROTEAN® TGX Stain-Free™ Protein Gels	Bio-Rad	Cat#4568094
4–20% Criterion™ TGX Stain-Free™ Protein Gel	Bio-Rad	Cat#5678094
GFP-Trap Magnetic Agarose	Chromotek	Cat#gtma-20
Anti-v5 agarose affinity gel	Sigma-Aldrich	Cat#A7345
Anti-FLAG® M2 Magnetic Beads	Sigma-Aldrich	Cat#M8823
Nunc™ Lab-Tek™ chambered coverglass	Thermo Fisher Scientific	Cat#155411PK
Lipofectamine™ 3000 Transfection Reagent	Thermo Fisher Scientific	Cat#L3000015
Experimental Models: Organisms/Strains		
Cib2^{tm1a}	EUCOMM	
Cib3^{KO}	This study	N/A
cib2^{idc21} zebrafish	This study	N/A
cib3^{idc22} zebrafish	This study	N/A
Tg(myo6b:GCaMP6s-CAAX)^{idc1} zebrafish	(Sheets et al., 2017)	ZDB-ALT-170113-3

609

610 **Mouse strains and husbandry**

611 *Cib2*^{KO} mice: *Cib2* $^{tm1a(EUCOMM)Wtsi}$ mice were obtained from the EUCOMM repository and

612 maintained on C57BL/6 N background. A gene trap cassette containing lacZ and neomycin

613 resistance genes flanked by FRT sites was inserted downstream of exon 3, with exon 4 flanked
614 by loxP sites.

615 *Cib3^{KO} mice: Cib3* knockout mice were generated using CRISPR/Cas9 technology. An
616 indel in exon 4 of *Cib3* was introduced leading to a nonsense mutation and a premature stop at
617 the protein level (p.Asp54*). Primers used to genotype Cib3 mutant mice were F:
618 GTAGGGGCATGGATAACATCTG and R: GTTGAATGCTTGTCTCCCCAGG. *Cib3^{KO}*
619 mice were backcrossed using C57Bl6/JN *Cib2^{KO}* mice for several generations. *Cib3* allele was
620 validated at the genomic, RNA messenger, and protein level.

621 Animals were group-housed with their littermates on a 12:12 h light: dark cycle at 20°C
622 with ad libitum access to food and water. All animal procedures were approved by the
623 Institutional Animal Care and Use Committees (IACUCs) at University of Maryland (protocol
624 #0420002) and at Harvard Medical School (protocol #00001240).

625

626 **Western blot and qPCR in mice**

627 Mouse heart tissues were homogenized in CHAPS buffer containing 1X protease inhibitors,
628 1 mM Na orthovanadate, 10 mM Na glycerophosphate, and 10 mM NaF. Equivalent protein
629 concentrations were fractionated on a 4–20% Bis–Tris gel (Invitrogen) and transferred to
630 polyvinylidene fluoride (PVDF) membrane (Millipore). Membranes were blocked and then
631 probed with the rabbit anti-CIB2 (1:500), CIB3 (1:500), and GAPDH (1:500) overnight at 4°C,
632 followed by three washes of 30 min each in 1X TBST. After washing, blots were incubated
633 with horseradish peroxidase-conjugated anti-rabbit antibody (1:1000, Sigma NA934V, Lot #
634 17640116) for 2 h at room temperature, followed by detection using the ECL Prime Western
635 Blotting System (Thermo Fisher Scientific 32,106).

636 RNAs from brain were extracted from *Cib2;Cib3* mutant and control mice using the
637 Ribopure kit (Ambion). SMARTScribe Reverse Transcriptase kit (Clontech) was used to

638 generate cDNAs, and SYBRgreen technology (Qiagen) was used to perform the qPCR. The
639 following primers were used to amplify *Cib2* and *Cib3*: Cib2_exon4_F:
640 CTCTGTGCTCTGCGAATCAG, Cib2_exon5_R: GGCCAGCGTCATCTCTAAGT,
641 Cib3_exon3_F: TGGTGCCTCTTGACTACACG, Cib3_exon5_R:
642 CAGCACCTTCTCACAGACCA. *hprt* amplification was used to normalize the samples:
643 hprt_exon8_F: TGTTGTTGGATATGCCCTTG, hprt_exon9_R:
644 GGCTTTGTATTTGGCTTTTCC.
645
646 **Quantification of VOR and OKR in mice**
647 Surgical techniques and experimental setup have been previously described (Beraneck and
648 Cullen, 2007). Eye movement data were collected using an infrared video system (ETL-200,
649 ISCAN system). The rotational velocity of the turntable (head velocity) was measured using a
650 MEMS sensor (MPU-9250, SparkFun Electronics). Eye movements during OKR were evoked
651 by sinusoidal rotations of a visual surround (vertical black and white stripes, visual angle width
652 of 5°) placed around the turntable at frequencies 0.2, 0.4, 0.8, 1, and 2 Hz with peak velocities
653 of ±16◦/s. To record VOR responses, the turntable was rotated at sinusoidal frequencies 0.2,
654 0.4, 0.8, 1, and 2 Hz with peak velocities of ±16◦/s in both light and dark. In the light condition,
655 the visual surround remained stationary, whereas in the dark condition, both the visual surround
656 and turntable rotated in phase. Head and eye movement signals were low-passed filtered at 125
657 Hz and sampled at 1 kHz. Eye position data were differentiated to obtain velocity traces. Cycles
658 of data with quick phases were excluded from the analysis. Least-square optimization
659 determined the VOR and OKN gains and phases (Beraneck et al., 2008) plotted as mean ±
660 standard deviation (SD) against all frequencies for all mice. $Cib2^{+/+}$; $Cib3^{KO/KO}$ (n = 4),
661 $Cib2^{KO/+}$; $Cib3^{KO/KO}$ (n = 5), and $Cib2^{KO/KO}$; $Cib3^{KO/KO}$ (n = 4) mice were tested for all

662 frequencies. Two-way ANOVAs and Bonferroni post hoc tests were used to test statistical
663 significance.
664
665 **Mouse rotarod test**
666 *Cib2*$^{+/+}$;*Cib3*$^{KO/KO}$ (n = 6), *Cib2*$^{KO/+}$;*Cib3*$^{KO/KO}$ (n = 6), and *Cib2*$^{KO/KO}$;*Cib3*$^{KO/KO}$ (n = 6) mice
667 were used. Motorized rotating rod (Rotarod, IITC Life Science) was programmed to accelerate
668 from 4 rpm to 40 rpm with a ramp of 300 s for each test trial. The time taken for a mouse to
669 fall off the rotarod was recorded. Three trials were performed each day for 5 consecutive days.
670 First day (day 0) was considered the training day.
671
672 **Quantification of head motion in mice**
673 Head motion was recorded in mice via a miniature motion sensor (MPU-9250, TDK
674 Corporation) attached to the top of the skull. The motion sensor recorded 3-axis linear
675 acceleration (i.e., fore-aft, lateral, and vertical) and 3-axis angular velocity (roll, pitch, and
676 yaw) at 100 Hz sampling rate. The power spectra of the motion signals in all six dimensions
677 were computed using Welch's averaged periodogram with nfft = 512 and a Bartlett window
678 (pwelch function, MATLAB, MathWorks).
679
680 **Circling behavior in mice**
681 Mice were placed in a cylindrical-shape container (27 cm in diameter, 30 cm in height) and
682 their behavior were recorded using a cell-phone camera. The number of rotations made during
683 120-second recording were counted offline by watching the recorded videos. A rotation is
684 defined as a completed 360-degree rotation of the mouse's heading.
685
686 **Immunostaining in mice**

687 The cochlear and vestibular sensory epithelia were isolated, fine dissected and permeabilized
688 in 0.25% Triton X-100 for 1 h and blocked with 10% normal goat serum in PBS for 1 h. The
689 tissue samples were probed with primary antibody overnight and after three washes were
690 incubated with the secondary antibody for 45 min at room temperature. Rhodamine phalloidin
691 or Alexa fluor phalloidin 488 were used at a 1:250 dilution for F-actin labeling. Nuclei were
692 stained with DAPI (Molecular Probes). Images were acquired using either LSM 700 laser
693 scanning confocal microscope (Zeiss, Germany) with a 63× 1.4 NA or 100× 1.4 NA oil
694 immersion objectives or Leica SP8 laser scanning confocal microscope with a 100× 1.44 NA
695 objective lens. Stacks of confocal images were acquired with a Z step of 0.05-0.5 µm and
696 processed using ImageJ software (National Institutes of Health). Experiments were repeated at
697 least 3 times, using at least three different animals.
698
699 **FM 1-43 dye uptake experiments in mice**
700 In the Ahmed lab, cochlear explants from *Cib2* and *Cib3* mutant mice were dissected at
701 postnatal day 5 (P5) and cultured in a glass-bottom petri dish (MatTek, Ashland, MA). They
702 were maintained in Dulbecco's modified Eagle medium (DMEM) supplemented with 10% FBS
703 (Life Technologies) for 2 days at 37 °C and 5% CO_2. Explants were incubated for 10 s with
704 3 µM FM 1-43, washed three times with Hank's balanced salt solution, and imaged live using
705 a Zeiss LSM 700 scanning confocal microscope.
706 In the Holt Lab, P60 mice were injected intraperitoneally with 5 mg/g mouse weight of
707 FM 1-43FX fixable form as previously described (Meyers et al., 2003). Tissue was collected
708 after ~24 h and fixed for 1 h at 25 °C in 4%PFA/1X PBS protected from light. Tissue was then
709 transferred into 120 mM EDTA pH 7.4 for 48-72 h protected from light. Then tissue was
710 transferred to 1XPBS, dissected, incubated in 1:1000 dilution of Phalloidin (Invitrogen),
711 washed three times in 1XPBS and mounted under glass coverslips for microscopy. Imaging

712 was completed using a 20× objective on a Zeiss 800 confocal microscope with laser intensity,
713 detector gain, and post processing set equally for each sample.
714
715 **ABR measurements in mice**
716 Hearing thresholds of *Cib2* and *Cib3* mutant mice (n = 5–10 each genotype) were evaluated by
717 recording ABRs. All ABR recordings, including broadband clicks and tone-burst stimuli at
718 three frequencies (8, 16, and 32 kHz), were performed using an auditory-evoked potential RZ6-
719 based auditory workstation (Tucker-Davis Technologies) with high frequency transducer
720 RA4PA Medusa PreAmps. Maximum sound intensity tested was 100 dB SPL. TDT system III
721 hardware and BioSigRZ software (Tucker Davis Technology) were used for stimulus
722 presentation and response averaging.
723
724 **Zebrafish strains and husbandry**
725 Zebrafish (*Danio* rerio) were grown at 28°C using standard methods. Zebrafish were
726 maintained in a Tubingen or TAB background. Larvae were raised in E3 embryo medium
727 (5 mM NaCl, 0.17 mM KCl, 0.33 mM $CaCl_2$, and 0.33 mM $MgSO_4$, buffered in HEPES, pH
728 7.2). Zebrafish work at the National Institute of Health (NIH) was approved by the Animal Use
729 Committee at the NIH under animal study protocol #1362-13. All experiments were performed
730 on larvae at 5-6 days post fertilization (dpf). At this age sex determination is not possible.
731 Neuromasts (L1-L5) in the primary posterior lateral line were used for our analyses. For Ca^{2+}
732 imaging the following transgenic line was used: *Tg(myo6b:memGCaMP6s)*^{idc1} (Jiang et al.,
733 2017).
734 *Cib2*^{idc21} and *cib3*^{idc22} mutants were generated in-house using CRISPR-Cas9 technology
735 as previously described (Varshney et al., 2016). Exon 3 and exon 6 were targeted for *cib2* and

736 *cib3* respectively. Guides for *cib2* and *cib3* are as follows: 5'-
737 GGAGGAGCTTACACCAG(AGG)-3' and 5'-GGAAATCCTCCAGAGAAAGG(CGG)-3'.
738 Founder fish were identified using fragment analysis of fluorescent PCR products (Varshney
739 et al., 2016). Founder fish containing a 10 bp insertion in *cib2* 5'-
740 GCTTACACCA(CCTTTGGTAG)GAGGAGGTTA-3' and a 4 bp deletion in *cib3* 5'-
741 TGGCCGCCT(TTCT)CTGGAGG-3' were propagated and selected for analysis. After
742 behavior or imaging analyses, genotypes were confirmed using standard PCR and sequencing.
743 The following primers were used for genotyping: *cib2*_FWD 5'-
744 ACTGAAGCAACTCCTTTTGTGG-3' and *cib2*_REV 5'-GAACCATGCATTTTTACAGC-
745 3' and *cib3*_FWD 5'-ATAGTCTCTCCATCTATAGACT-3' and *cib3*_REV 5'-
746 TTTTAGGGTGAAATAAAACAGA-3'. Crosses of *cib2*$^{+/-}$;*cib3*$^{-/-}$ X *cib2*$^{+/-}$;*cib3*$^{+/-}$ or *cib2*$^{-/-}$
747 ;*cib3*$^{+/-}$ X *cib2*$^{+/-}$;*cib3*$^{+/-}$ adults were used to propagate larvae for our analyses. All controls or
748 siblings are double heterozygous animals. Larvae were chosen at random, except for *cib2;cib3*
749 homozygous mutants which, similar to other zebrafish mutants with hearing and balance
750 defects, had no swim bladder and no acoustic startle response.
751

752 **Labeling zebrafish hair cells with FM 1-43, FM 4-64, and FM 1-43FX**

753 To label lateral-line hair cells with FM 1-43, larvae were immersed in 1 μM FM 1-43
754 (ThermoFisher, T3163) in E3 for 30 s, and then washed 3 times in E3. After washing, larvae
755 were mounted in 1% low melt agarose containing an anesthetic, 0.02% tricaine
756 methanesulfonate (Syndel, ANADA 200-226). FM 1-43 labeled hair cells were then imaged
757 on an A1 Nikon upright laser-scanning confocal microscope with a 60× 1.0 NA water
758 objective. FIJI was used to process image Z-stacks. To estimate the number of hair cells per
759 neuromast, laser scanning DIC images were used to count the number of hair bundles per
760 neuromast. To quantify FM 1-43 label, a 5 μm circular region of interest (ROI) was placed on

761 the soma of each hair cell with a hair bundle in the DIC image. These ROIs were used to
762 quantify the mean FM 1-43 intensity per hair cell. These intensity values were averaged to
763 calculate the average FM 1-43 intensity per neuromast.

764 FM 4-64 (ThermoFisher, T13320) was used to label hair cells in the crista within the
765 zebrafish inner ear. For this labeling, *Tg(myo6b:memGCaMP6s)*^{idc1} larvae were mounted on
766 their side on Sylgard chamber in E3 embryo media containing 0.02% MESAB. Approximately
767 2-3 nL of 10 µM FM 4-64 in 0.1 M KCl were injected into the otic capsule as previously
768 described (Smith et al., 2020). FM 4-64 labeled hair cells of the medial crista were then imaged
769 on an A1 Nikon upright laser-scanning confocal microscope with a 25× 1.10 NA or 60× 1.0
770 NA water objective. FIJI was used to process image Z-stacks. To assess tall versus short hair
771 cells in each crista *memGCaMP6s* label was used.

772 To correlate hair bundle orientation in lateral line hair cells with intact
773 mechanotransduction, larvae were immersed in 3 µM FM 1-43FX (ThermoFisher, F25255) in
774 E3 for 30 s, and then washed 3 times in E3. After washing, larvae were fixed with 4%
775 paraformaldehyde in PBS at 4°C overnight. After fixation, larvae were washed 4 × 5 min in
776 0.1% Tween in PBS (PBST). Larvae were then placed in blocking solution (2% goat serum,
777 1% bovine serum albumin, 2% fish skin gelatin in PBS + 0.3% triton) for 2 h at room
778 temperature. After block Alexa Fluor 633 Phalloidin (ThermoFisher, A22284) was added at
779 1:100 in PBST. Larvae were incubated for 4 h at room temperature and then washed 4 × 5 min
780 in PBST. Larvae were mounted on glass slides with Prolong Gold (ThermoFisher Scientific)
781 using No. 1.5 coverslips. To image hair bundle orientation and FM 1-43FX label in lateral-line
782 hair cells, a Zeiss LSM780 confocal microscope with Airyscan was used. Hair cells were
783 imaged using a 63× 1.3 NA oil objective and processed with an Airyscan processing factor of
784 7.0. For analysis, Z-stacks were max-projected in FIJI. Images were background subtracted

785 using a rolling ball correction. Hair cells with a FM 1-43FX intensity more than twice the
786 background intensity were scored as FM 1-43FX positive.
787
788 **Zebrafish Ca^{2+} imaging and behavior**
789 For imaging of mechanosensitive Ca^{2+} signals in neuromast hair bundles,
790 *Tg(myo6b:memGCaMP6s)* animals were mounted on their side on Sylgard chamber in E3
791 embryo media containing 0.2% MESAB (Lukasz and Kindt, 2018). Larvae were then pinned
792 and a solution containing α-bungarotoxin (125 μM, Tocris) was injected into the heart cavity
793 for paralysis during imaging. After paralysis, larvae were immersed in extracellular imaging
794 solution (in mM: 140 NaCl, 2 KCl, 2 $CaCl_2$, 1 $MgCl_2$ and 10 HEPES, pH 7.3, OSM 310 +/-
795 10). To image Ca^{2+} signals in the hair bundles we used a Bruker Swept-Field confocal system
796 equipped with a Rolera EM-C2 CCD camera (QImaging, Surrey, Canada) and a Nikon CFI
797 Fluor 60×1.0 NA water immersion objective as previously described (Q. Zhang et al., 2018).
798 The system includes a band-pass 488/561 nm filter set (59904-ET, Chroma) and is controlled
799 using Prairie View software (Bruker Corporation). A piezoelectric motor (PICMA P-882.11-
800 888.11 series, PI Instruments) attached to the objective and used to acquire 5-plane Z-stacks
801 every 0.5 μm using a 35 μm slit at a 50-Hz frame rate for a 10-Hz volume rate. A fluid-jet
802 composed of a glass capillary attached to a pressure clamp system (HSPC-2-SB, ALA) was
803 used to deliver a 500-ms anterior and posterior step stimulation to deflect hair bundles along
804 their axis of sensitivity.
805 To quantify GCaMP6s fluorescent intensity changes during stimulation, we registered
806 the Z-stacks and then average projected the Z-stacks into a single plane. We then loaded the
807 projected images into FIJI and used the Time Series Analyzer V3 plugin to create circular ROIs
808 with a ~1.7 μm diameter. ROIs were placed on the center of each individual bundle. We then
809 measured and plotted change in the mean intensity ($\Delta F/F_0$) within the region during the

810 recording period. The mean intensity within each ROI was computed for each hair bundle. A
811 hair bundle with a signal magnitude (peak value of intensity change upon stimulation) above
812 10% $\Delta F/F_0$ was considered mechanosensitive. To create the AVG hair bundle GCaMP6s
813 ($\Delta F/F_0$) per neuromast plot in Figure 5-figure supplement 1C, only traces from
814 mechanosensitive cells were averaged.

815 A Zantiks MWP behavioral system was used to examine startle responses. The Zantiks
816 system tracked and monitored behavioral responses via a built-in infrared camera at 30 frames
817 per second. A 12-well plate was used to house larvae during behavioral analysis. Each well
818 was filled with E3 and 1 larva. All fish were acclimated in the plate within the Zantiks chamber
819 in dark for 15 min before each test. To induce startle, an integrated stepper motor was used to
820 drive a vibration-induced startle response. A vibrational stimulus that triggered a maximal %
821 of animals startling in controls without any tracking artifacts (due to the vibration) was used
822 for our analyses. Each larva was presented with the vibrational stimulus 5 times with 100 s
823 between trials. During the tracking and stimulation, a Cisco router connected to the Zantiks
824 system was used to relay *x*, *y* coordinates of each larva every frame. To qualify as a startle
825 response, a distance above 4 pixels or ~1.9 mm was required within 2 frames after stimulus
826 onset. Animals were excluded from our analysis if no tracking data was recorded for the animal.
827

828 **Zebrafish Statistics**

829 All data shown are mean ± standard error of the mean (SEM). All experiments were performed
830 on at least 4 animals and 8 neuromasts and 4 cristae. Behavior analysis and Ca^{2+} imaging was
831 repeated at least twice on two independent days. All statistical analysis was performed using
832 GraphPad Prism 8.0. A D'Agostino and Pearson test was used to test data for normality. A
833 one-way ANOVA with a Dunnett's correction for multiple comparisons was used to compare
834 differences between siblings and controls regarding the % of mechanosensitive hair cells,

835 number of hair cells, % of FM 1-43 positive hair cells, average FM 1-43 label. For proportion
836 of animals startling and comparisons for FM 1-43FX label, a Kruskal-Wallis test with a
837 Dunnett's correction for multiple comparisons was used.
838
839 **Expression and purification of bacterially expressed *hs* CIB2, CIB3, TMC1-IL1, and**
840 **TMC1-NT**
841 DNA sequences encoding for *hs* CIB2, CIB3, TMC1-IL1, and TMC1-NT were subcloned into
842 *NdeI* and *XhoI* sites of the pET21a vector. All DNA constructs were sequence verified. Protein
843 fragments were expressed in *Escherichia coli* BL21 Rosetta (DE3) (Novagen) cells, which
844 were cultured in LB or TB media, induced at OD_{600} ~0.4-0.6 with 1 mM IPTG and grown at
845 20°C or 30°C for ~16 h. Protein fragments for NMR were produced using the same cells
846 cultured in M9 minimal media supplemented with MEM vitamin solution (Gibco) and 1g/L
847 $^{15}NH_4Cl$ (Cambridge Isotopes) to produce uniformly labeled [U-^{15}N] protein. Cells were lysed
848 by sonication in denaturing buffer (20 mM Tris HCl, pH 7.5, 6 M guanidine hydrochloride, 10
849 mM $CaCl_2$, and 20 mM imidazole) or non-denaturing buffer (20 mM Tris HCl, pH 7.5, and 20
850 mM imidazole for *hs* TMC1-NT). The cleared lysates were loaded onto Ni-Sepharose (GE
851 Healthcare) and eluted with denaturing buffer or non-denaturing buffer supplemented with 500
852 mM imidazole. Denatured proteins were refolded using MWCO 2,000 membranes
853 (Spectra/Por 7) in dialysis buffer (400 mM Arg-HCl, 20 mM Tris-HCl, pH 7.5, 150 mM KCl,
854 50 mM NaCl, 2 mM $CaCl_2$, 2 mM DTT) for ~16 hr. Before starting refolding reactions (when
855 applicable), elution solutions were diluted to ~0.5 mg/mL using the denaturing buffer, and then
856 reduced by using 2 mM DTT in the diluted sample. Refolded and soluble proteins were
857 concentrated using Vivaspin 20 or Amicon 15 centrifugal concentrators (10 kDa, 5 kDa, or 3
858 kDa molecular weight cutoff) and further purified on Superdex S75 columns (GE Healthcare)

859 in SEC buffer (50 mM HEPES, pH 7.5, 126 mM KCl, 10 mM NaCl, 3 mM $CaCl_2$, 5 mM DTT).
860 Proteins were concentrated to ~0.5 mL for nuclear magnetic resonance (NMR) experiments.
861
862 **NMR**
863 Purified NMR samples were at concentrations of ~1.4 mM, ~0.2 mM, ~0.8 mM, and ~0.2 mM
864 for CIB2, CIB3, CIB2 + TMC1-IL1, and CIB3 + TMC1-IL1, respectively, in SEC buffer (50
865 mM HEPES, pH 7.5, 126 mM KCl, 10 mM NaCl, 3 mM $CaCl_2$, 5 mM DTT), supplemented
866 with 10% (v/v) D_2O and 0.2 mM 2,2-dimethyl-2-silapentane-5-sulphonate (DSS) for field-
867 frequency locking and chemical shift referencing. Two-dimensional ^{1}H-^{15}N TROSY-HSQC
868 spectra (Nietlispach, 2005) were recorded for each sample at 25°C on a Bruker Avance III HD
869 800 MHz spectrometer equipped with a 5 mm TXI cryoprobe with z-gradients. Data were
870 collected using 20 to 24 scans, 2,048 x 280 datapoints, and spectral widths of 17482.518 x
871 4054.298 Hz in the ^{1}H and ^{15}N dimensions, respectively. Data were processed and visualized
872 using NMRFx (Norris et al., 2016).
873
874 **Simulated Systems**
875 Models for monomeric *hs* TMC1 (residues 84 to 760; NCBI ID: NP_619636.2) and *hs* TMC2
876 (148 to 863; NCBI ID: NP_542789.2) in complex with full-length *hs* CIB2 (NCBI ID:
877 NP_006374.1) and *hs* CIB3 (NCBI ID: NP_473454.1), as well as truncated dimeric models of
878 *hs* TMC1 (residues 260 to 760; NCBI ID: NP_619636.2) and *hs* TMC2 (residues 324 to 863;
879 NCBI ID: NP_542789.2) were generated using AF2 (Evans et al., 2021; Jumper et al., 2021).
880 The TMC2 C-terminal end (residues 818 to 863) was truncated to match the C-terminal end of
881 TMC1. Using VMD (Humphrey et al., 1996), a model of dimeric *hs* TMC1 + *hs* CIB3-Ca^{2+}
882 was constructed by aligning the monomeric *hs* TMC1 + *hs* CIB3 complex to the
883 transmembrane region of the truncated dimeric *hs* TMC1 model. Coordinates for Ca^{2+} ions

884 were obtained by aligning the crystal structure of Mg^{2+}-bound *hs* CIB3 in complex with a *hs*
885 TMC1-IL1 peptide (PDB code: 6WUD) (Liang et al., 2021) to the AF2 model of monomeric
886 *hs* TMC1 + *hs* CIB3, then manually changing Mg^{2+} for Ca^{2+}. This model was minimized for
887 1,000 steps in vacuum using NAMD (Phillips et al., 2005) and the CHARMM36 force field
888 (Best et al., 2012; Huang and MacKerell, 2014; Vanommeslaeghe and MacKerell, 2015) and
889 served as a reference model for aligning other combinations of *hs* TMC1 or *hs* TMC2 with *hs*
890 CIB2 or *hs* CIB3. All models were either embedded into pure POPC or mixed membrane lipid
891 bilayers using CHARMM-GUI (Jo et al., 2009, 2008, 2007; Lee et al., 2019) as summarized
892 in Table supplement 1. The mixed membrane mimicked stereocilia membrane composition
893 (Zhao et al., 2012). The protein-lipid system was then solvated using TIP3P explicit water and
894 neutralized with 0.150 M KCl, representative of endolymph ionic concentration (Bosher and
895 Warren, 1978).
896
897 **Simulations using NAMD**
898 All-atom MD simulations were performed and analyzed using NAMD 2.13 (Phillips et al.,
899 2005) and the CHARMM36 force field with CMAP corrections (Best et al., 2012; Huang and
900 MacKerell, 2014; Vanommeslaeghe and MacKerell, 2015). For all systems, equilibrium
901 simulations consisted of 2,000 steps of minimization, 0.5 ns of dynamics with everything
902 excluding lipid tails fixed/constrained, 0.5 ns of dynamics with harmonic constraints applied
903 to the protein (1 kcal mol^{-1} $Å^{-2}$), 1 ns of free dynamics in the *NpT* ensemble (γ = 1 ps^{-1}), and up
904 to 100 ns of free dynamics in the *NpT* ensemble (γ = 0.1 ps^{-1}) prior to non-equilibrium
905 production runs. A piston period of 200 fs and a damping timescale of 50 fs was used for
906 pressure control and atomic coordinates were saved every 5 ps. All simulations were performed
907 at 310 K and 1 atmosphere of pressure by using the Langevin thermostat and Nosé-Hoover
908 Langevin pressure control. A 12-Å cutoff distance was employed with a force-based switching

909 function starting at 10 Å. Periodic boundary conditions and the PME method were used to
910 calculate long-range electrostatic interactions with a grid density greater than 1 $Å^{-3}$. An
911 integration timestep of 2 fs with electrostatic interactions computed every other timestep was
912 utilized for every simulation in tandem with the SHAKE algorithm for the constraint of
913 hydrogen atoms. A constant electric field was applied to all atoms in non-equilibrium
914 simulations with transmembrane potential (Gumbart et al., 2012).
915
916 **Simulations using Anton 2**
917 We used Anton 2, a massively parallel special purpose machine for MD simulations (Shaw et
918 al., 2014), to run simulations of *hs* TMC1 + *hs* CIB2-Ca^{2+} in POPC (simulations S1d-g; Table
919 supplement 1), *hs* TMC1 + *hs* CIB2 in POPC (simulations S2d-2g; Table supplement 1), *hs*
920 TMC1 in POPC (simulations S3d-g; Table supplement 1), and *hs* TMC1 + *hs* CIB2 in a mixed
921 membrane (simulations S4c-d; Table supplement 1). Coordinates of the pre-equilibrated
922 systems were converted to an Anton 2 compatible dms file format using the NAMDtoDMS.py
923 script provided by the Pittsburgh Supercomputing Center. Simulations used CHARMM36
924 forcefields and were performed in the *NpT* ensemble (310 K, 1 atm) using the multigrator
925 integration framework (Lippert et al., 2013) with a 2.5 fs integration timestep and saved every
926 120 ps. The MTK barostat and Nosé-Hoover thermostat was updated every 480 and 24 steps,
927 respectively. Semi-isotropic pressure coupling was used. Long range electrostatic interactions
928 were calculated using u-series electrostatics with a 64 × 64 × 64 grid. Van der Waals
929 interactions were calculated with a cutoff of 12 Å. Transmembrane voltages were generated by
930 applying a constant electric field to all atoms (Gumbart et al., 2012).
931
932 **Simulation analysis procedures and tools**

933 BSA was computed in VMD by measuring SASA for both TMC and CIB monomers, then
934 subtracting SASA for the complex. BSA for interacting molecules A and B were computed as
935 $BSA_{AB} = 1/2(SASA_A + SASA_B - SASA_{AB})$. RMSD values were computed in VMD using Cα
936 atoms and initial models as references, with alignments carried out using the corresponding
937 subdomains when indicated. VMD was used to analyze trajectories, render molecular images,
938 and create videos. Xmgrace and gnuplot were used to generate plots. Sequences for CIB and
939 TMC isoforms from various species were obtained from the NCBI protein database. Sequences
940 were aligned utilizing the MUSCLE algorithm within Geneious (Kearse et al., 2012). Aligned
941 sequences were loaded into JalView (Waterhouse et al., 2009) and colored based on a sequence
942 identity threshold of 45%. Ionic currents were computed by counting the number of crossing,
943 with conductance values estimated as in Walujkar et al., 2021.
944
945 **Resource Availability**
946 **Lead Contact**
947 Further information and requests for resources and reagents should be directed to the Lead
948 Contacts, Drs. Marcos Sotomayor (sotomayor.8@osu.edu) and Zubair M. Ahmed
949 (zmahmed@som.umaryland.edu).
950
951 **Materials availability**
952 Materials generated in this study, including strains, plasmids and clones, are freely available
953 from the Lead Contact upon request.
954
955 **Data and code availability**
956 This study did not generate any unique datasets or code.
957

958 **Acknowledgements**

959 We acknowledge Sakina Rehman for assistance with animal work, Neal Taliwal for assistance
960 with molecular cloning, Chunhua Yuan for assistance with initial nuclear magnetic resonance
961 experiments, and Collin R. Nisler and Harsha Mandayam Bharathi for assistance with
962 simulations analyses. Simulations were carried out at the Ohio Supercomputer Center (OSC
963 grants PAS1037 and PAA0217) and the Pittsburgh Supercomputer Center (PSC Anton 2 grant
964 MCB150024P). Nuclear magnetic resonance data were acquired at the Ohio State University
965 Campus Chemical Instrument Center. This study was supported by NIH/NIDCD grants
966 R01DC015271 to M.S. and R01DC012564 to Z.M.A. and G.I.F., an Intramural Research
967 Program Grant 1ZIADC000085-01 to K.S.K., and NIH grants UF1NS111695, R01DC018304,
968 R01DC002390, R01DC018061 to K.E.C.

969

970 **Additional information**

971 **Author contributions**

972 Z.M.A., K.S.K., and M.S. conceived the studies. A.P.J.G. carried out all audiometric
973 recordings in mice, immunolocalization studies, cochlear and vestibular explant cultures, FM
974 1-43 uptake experiment on mouse tissues, RT-qPCRs, exploratory testing, *Cib2* and *Cib3*
975 mouse phenotyping and genotyping, cloning of CIB2 and CIB3 in pET21a vectors. K.S.K.
976 conducted zebrafish FM 1-43, FM 4-64, FM 1-43FX labeling, Ca^{2+} imaging and
977 immunostaining. A.J.B. created the *cib2* and *cib3* zebrafish mutants. R.A.R. did the zebrafish
978 behavioral studies. W-H.W. did the cloning and mutagenesis of CIB and TMC constructs,
979 protein expression and purification for NMR experiments, as well as model building and
980 molecular dynamics simulations. J.S.M. did NMR experiments and NMR data processing.
981 E.M.R. performed FM 1-43 uptake experiments in mice. J.M.L. and S.W. did model building.
982 M.P.F. supervised NMR experiments and project. M.S. supervised project and assisted with

983 cloning, strategies for protein refolding, model building, and simulations. H.H.V.C. and O.A.Z.
984 performed VOR, OKN measurements and vestibular function evaluation of mice. J.R.H.,
985 analyzed the mouse FM 1-43 experiments data, provided supervision and resources. S.R., and
986 Z.M.A., supervised the project, reviewed and interpreted the results, provided resources. All
987 authors contributed to data analysis. A.P.J.G, K.S.K, K.C, M.S. and Z.M.A. wrote the
988 manuscript. All authors edited the manuscript and approved for submission.

989 **References**

990 Ahmed ZM, Goodyear R, Riazuddin Saima, Lagziel A, Legan PK, Behra M, Burgess SM,
991 Lilley KS, Wilcox ER, Riazuddin Sheikh, Griffith AJ, Frolenkov GI, Belyantseva IA,
992 Richardson GP, Friedman TB. 2006. The tip-link antigen, a protein associated with the
993 transduction complex of sensory hair cells, is protocadherin-15. *J Neurosci* **26**:7022–
994 7034. doi:10.1523/JNEUROSCI.1163-06.2006

995 Akyuz N, Karavitaki KD, Pan B, Tamvakologos PI, Brock KP, Li Y, Marks DS, Corey DP.
996 2022. Mechanical gating of the auditory transduction channel TMC1 involves the fourth
997 and sixth transmembrane helices. *Sci Adv* **8**:eabo1126. doi:10.1126/sciadv.abo1126

998 Ballesteros A, Fenollar-Ferrer C, Swartz KJ. 2018. Structural relationship between the
999 putative hair cell mechanotransduction channel TMC1 and TMEM16 proteins. *Elife* **7**.
1000 doi:10.7554/eLife.38433

1001 Beraneck M, Cullen KE. 2007. Activity of vestibular nuclei neurons during vestibular and
1002 optokinetic stimulation in the alert mouse. *J Neurophysiol* **98**:1549–1565.
1003 doi:10.1152/jn.00590.2007

1004 Beraneck M, McKee JL, Aleisa M, Cullen KE. 2008. Asymmetric recovery in cerebellar-
1005 deficient mice following unilateral labyrinthectomy. *J Neurophysiol* **100**:945–958.
1006 doi:10.1152/jn.90319.2008

1007 Best RB, Zhu X, Shim J, Lopes PE, Mittal J, Feig M, Mackerell Jr. AD. 2012. Optimization
1008 of the additive CHARMM all-atom protein force field targeting improved sampling of
1009 the backbone phi, psi and side-chain chi(1) and chi(2) dihedral angles. *J Chem Theory*
1010 *Comput* **8**:3257–3273. doi:10.1021/ct300400x

1011 Beurg M, Cui R, Goldring AC, Ebrahim S, Fettiplace R, Kachar B. 2018. Variable number of

1012 TMC1-dependent mechanotransducer channels underlie tonotopic conductance
1013 gradients in the cochlea. *Nat Commun* **9**:2185. doi:10.1038/s41467-018-04589-8

1014 Beurg M, Fettiplace R, Nam J-H, Ricci AJ. 2009. Localization of inner hair cell
1015 mechanotransducer channels using high-speed calcium imaging. *Nat Neurosci* **12**:553–
1016 558. doi:10.1038/nn.2295

1017 Beurg M, Nam J-H, Fettiplace R. 2021. The speed of the hair cell mechanotransducer
1018 channel revealed by fluctuation analysis. *J Gen Physiol* **153**. doi:10.1085/jgp.202112959

1019 Booth KT, Kahrizi K, Babanejad M, Daghagh H, Bademci G, Arzhangi S, Zareabdollahi D,
1020 Duman D, El-Amraoui A, Tekin M, Najmabadi H, Azaiez H, Smith RJ. 2018. Variants
1021 in CIB2 cause DFNB48 and not USH1J. *Clin Genet* **93**:812–821. doi:10.1111/cge.13170

1022 Bosher SK, Warren RL. 1978. Very low calcium content of cochlear endolymph, an
1023 extracellular fluid. *Nature* **273**:377–378. doi:10.1038/273377a0

1024 Chen Z, Zhu S, Kindig K, Wang S, Chou SW, Davis RW, Dercoli MR, Weaver H, Stepanyan
1025 R, McDermott BM. 2020. Tmc proteins are essential for zebrafish hearing where Tmc1
1026 is not obligatory. *Hum Mol Genet* **29**:2004–2021. doi:10.1093/HMG/DDAA045

1027 Chou SW, Chen Z, Zhu S, Davis RW, Hu J, Liu L, Fernando CA, Kindig K, Brown WC,
1028 Stepanyan R, McDermott BM. 2017. A molecular basis for water motion detection by
1029 the mechanosensory lateral line of zebrafish. *Nat Commun* **8**. doi:10.1038/s41467-017-
1030 01604-2

1031 Cullen KE. 2019. Vestibular processing during natural self-motion: implications for
1032 perception and action. *Nat Rev Neurosci* **20**:346–363. doi:10.1038/s41583-019-0153-1

1033 Cunningham CL, Qiu X, Wu Z, Zhao B, Peng G, Kim YH, Lauer A, Müller U. 2020. TMIE
1034 Defines Pore and Gating Properties of the Mechanotransduction Channel of Mammalian

1035 Cochlear Hair Cells. *Neuron* **107**:126-143.e8. doi:10.1016/j.neuron.2020.03.033

1036 Dal Cortivo G, Marino V, Iacobucci C, Vallone R, Arlt C, Rehkamp A, Sinz A, Dell'Orco D.
1037 2019. Oligomeric state, hydrodynamic properties and target recognition of human
1038 Calcium and Integrin Binding protein 2 (CIB2). *Sci Rep* **9**. doi:10.1038/s41598-019-
1039 51573-3

1040 Effertz T, Becker L, Peng AW, Ricci AJ. 2017. Phosphoinositol-4,5-bisphosphate regulates
1041 auditory hair-cell mechanotransduction-channel pore properties and fast adaptation. *J*
1042 *Neurosci* **37**:11632–11646. doi:10.1523/JNEUROSCI.1351-17.2017

1043 Erickson T, Morgan CP, Olt J, Hardy K, Busch-Nentwich E, Maeda R, Clemens R, Krey JF,
1044 Nechiporuk A, Barr-Gillespie PG, Marcotti W, Nicolson T. 2017. Integration of Tmc1/2
1045 into the mechanotransduction complex in zebrafish hair cells is regulated by
1046 Transmembrane O-methyltransferase (Tomt). *Elife* **6**. doi:10.7554/eLife.28474

1047 Ernest S, Rauch GJ, Haffter P, Geisler R, Petit C, Nicolson T. 2000. Mariner is defective in
1048 myosin VIIA: A zebrafish model for human hereditary deafness. *Hum Mol Genet*
1049 **9**:2189–2196. doi:10.1093/hmg/9.14.2189

1050 Evans R, O'Neill M, Pritzel A, Antropova N, Senior A, Green T, Žídek A, Bates R,
1051 Blackwell S, Yim J, Ronneberger O, Bodenstein S, Zielinski M, Bridgland A,
1052 Potapenko A, Cowie A, Tunyasuvunakool K, Jain R, Clancy E, Kohli P, Jumper J,
1053 Hassabis D. 2021. Protein complex prediction with AlphaFold-Multimer. *bioRxiv*
1054 2021.10.04.463034. doi:10.1101/2021.10.04.463034

1055 Fettiplace R. 2017. Hair cell transduction, tuning, and synaptic transmission in the
1056 mammalian cochlea. *Compr Physiol* **7**:1197–1227. doi:10.1002/cphy.c160049

1057 Fettiplace R, Furness DN, Beurg M. 2022. The conductance and organization of the TMC1-

1058 containing mechanotransducer channel complex in auditory hair cells. *Proc Natl Acad*
1059 *Sci U S A* **119**:e2210849119. doi:10.1073/pnas.2210849119

1060 Frolenkov GI, Belyantseva IA, Friedman TB, Griffith AJ. 2004. Genetic insights into the
1061 morphogenesis of inner ear hair cells. *Nat Rev Genet* **5**:489–498. doi:10.1038/nrg1377

1062 Giese APJ, Tang YQ, Sinha GP, Bowl MR, Goldring AC, Parker A, Freeman MJ, Brown
1063 SDM, Riazuddin S, Fettiplace R, Schafer WR, Frolenkov GI, Ahmed ZM. 2017. CIB2
1064 interacts with TMC1 and TMC2 and is essential for mechanotransduction in auditory
1065 hair cells. *Nat Commun* **8**. doi:10.1038/s41467-017-00061-1

1066 Gillespie PG, Müller U. 2009. Mechanotransduction by hair cells: models, molecules, and
1067 mechanisms. *Cell* **139**:33–44. doi:10.1016/j.cell.2009.09.010

1068 Gleason MR, Nagiel A, Jamet S, Vologodskaia M, López-Schier H, Hudspeth AJ. 2009. The
1069 transmembrane inner ear (Tmie) protein is essential for normal hearing and balance in
1070 the zebrafish. *Proc Natl Acad Sci U S A* **106**:21347–52. doi:10.1073/pnas.0911632106

1071 Gopal SR, Chen DHC, Chou SW, Zang J, Neuhauss SCF, Stepanyan R, McDermott BM,
1072 Alagramam KN. 2015. Zebrafish models for the mechanosensory hair cell dysfunction
1073 in usher syndrome 3 reveal that Clarin-1 is an essential hair bundle protein. *J Neurosci*
1074 **35**:10188–10201. doi:10.1523/JNEUROSCI.1096-15.2015

1075 Gumbart J, Khalili-Araghi F, Sotomayor M, Roux B. 2012. Constant electric field
1076 simulations of the membrane potential illustrated with simple systems. *Biochim Biophys*
1077 *Acta - Biomembr* **1818**:294–302. doi:10.1016/j.bbamem.2011.09.030

1078 Huang H, Bogstie JN, Vogel HJ. 2012. Biophysical and structural studies of the human
1079 calcium-and integrin-binding protein family: Understanding their functional similarities
1080 and differences. *Biochem Cell Biol* **90**:646–656. doi:10.1139/o2012-021

1081 Huang J, MacKerell ADJ. 2014. CHARMM36 all-atom additive protein force field:
1082 Validation based on comparison to NMR data. *J Comput Chem* **34**:2135–2145.
1083 doi:10.1002/jcc.23354.CHARMM36

1084 Humphrey W, Dalke A, Schulten K. 1996. VMD: Visual molecular dynamics. *J Mol Graph*
1085 **14**:33–38. doi:10.1016/0263-7855(96)00018-5

1086 Jeong H, Clark S, Goehring A, Dehghani-Ghahnaviyeh S, Rasouli A, Tajkhorshid E, Gouaux
1087 E. 2022. Structures of the TMC-1 complex illuminate mechanosensory transduction.
1088 *Nature* **610**:796–803. doi:10.1038/s41586-022-05314-8

1089 Jiang T, Kindt K, Wu DK. 2017. Transcription factor emx2 controls stereociliary bundle
1090 orientation of sensory hair cells. *Elife* **6**:1–26. doi:10.7554/eLife.23661

1091 Jo S, Kim T, Im W. 2007. Automated builder and database of protein/membrane complexes
1092 for molecular dynamics simulations. *PLoS One* **2**. doi:10.1371/journal.pone.0000880

1093 Jo S, Kim T, Iyer VG, Im W. 2008. CHARMM-GUI: A web-based graphical user interface
1094 for CHARMM. *J Comput Chem* **29**:1859–1865. doi:10.1002/jcc.20945

1095 Jo S, Lim JB, Klauda JB, Im W. 2009. CHARMM-GUI membrane builder for mixed bilayers
1096 and its application to yeast membranes. *Biophys J* **97**:50–58.
1097 doi:10.1016/j.bpj.2009.04.013

1098 Jojoa-Cruz S, Saotome K, Murthy SE, Tsui CCA, Sansom MS, Patapoutian A, Ward AB.
1099 2018. Cryo-EM structure of the mechanically activated ion channel OSCA1.2. *Elife* **7**.
1100 doi:10.7554/eLife.41845

1101 Jumper J, Evans R, Pritzel A, Green T, Figurnov M, Ronneberger O, Tunyasuvunakool K,
1102 Bates R, Žídek A, Potapenko A, Bridgland A, Meyer C, Kohl SAA, Ballard AJ, Cowie
1103 A, Romera-Paredes B, Nikolov S, Jain R, Adler J, Back T, Petersen S, Reiman D,

1104 Clancy E, Zielinski M, Steinegger M, Pacholska M, Berghammer T, Bodenstein S,
1105 Silver D, Vinyals O, Senior AW, Kavukcuoglu K, Kohli P, Hassabis D. 2021. Highly
1106 accurate protein structure prediction with AlphaFold. *Nature* 1–11. doi:10.1038/s41586-
1107 021-03819-2

1108 Karplus M, Petsko GA. 1990. Molecular dynamics simulations in biology. *Nature* **347**:631–
1109 9. doi:10.1038/347631a0

1110 Kawashima Y, Géléoc GSG, Kurima K, Labay V, Lelli A, Asai Y, Makishima T, Wu DK,
1111 Della Santina CC, Holt JR, Griffith AJ. 2011. Mechanotransduction in mouse inner ear
1112 hair cells requires transmembrane channel-like genes. *J Clin Invest* **121**:4796–809.
1113 doi:10.1172/JCI60405

1114 Kawashima Y, Kurima K, Pan B, Griffith AJ, Holt JR. 2015. Transmembrane channel-like
1115 (TMC) genes are required for auditory and vestibular mechanosensation. *Pflügers Arch -*
1116 *Eur J Physiol* **467**:85–94. doi:10.1007/s00424-014-1582-3

1117 Kazmierczak P, Sakaguchi H, Tokita J, Wilson-Kubalek EM, Milligan RA, Müller U, Kachar
1118 B. 2007. Cadherin 23 and protocadherin 15 interact to form tip-link filaments in sensory
1119 hair cells. *Nature* **449**:87–91. doi:10.1038/nature06091

1120 Kearse M, Moir R, Wilson A, Stones-Havas S, Cheung M, Sturrock S, Buxton S, Cooper A,
1121 Markowitz S, Duran C, Thierer T, Ashton B, Meintjes P, Drummond A. 2012. Geneious
1122 Basic: an integrated and extendable desktop software platform for the organization and
1123 analysis of sequence data. *Bioinformatics* **28**:1647–9. doi:10.1093/bioinformatics/bts199

1124 Kindig K, Stepanyan R, Kindt KS, McDermott BM. 2023. Asymmetric mechanotransduction
1125 by hair cells of the zebrafish lateral line. *Curr Biol* **33**:1295-1307.e3.
1126 doi:10.1016/j.cub.2023.02.033

1127 Lee Jumin, Patel DS, Ståhle J, Park SJ, Kern NR, Kim S, Lee Joonseong, Cheng X, Valvano
1128 MA, Holst O, Knirel YA, Qi Y, Jo S, Klauda JB, Widmalm G, Im W. 2019. CHARMM-
1129 GUI Membrane Builder for Complex Biological Membrane Simulations with
1130 Glycolipids and Lipoglycans. *J Chem Theory Comput* **15**:775–786.
1131 doi:10.1021/acs.jctc.8b01066

1132 Liang X, Qiu X, Dionne G, Cunningham CL, Pucak ML, Peng G, Kim YH, Lauer A, Shapiro
1133 L, Müller U. 2021. CIB2 and CIB3 are auxiliary subunits of the mechanotransduction
1134 channel of hair cells. *Neuron*. doi:10.1016/j.neuron.2021.05.007

1135 Lippert R a, Predescu C, Ierardi DJ, Mackenzie KM, Eastwood MP, Dror RO, Shaw DE.
1136 2013. Accurate and efficient integration for molecular dynamics simulations at constant
1137 temperature and pressure. *J Chem Phys* **139**:164106. doi:10.1063/1.4825247

1138 Liu X, Wang J, Sun L. 2018. Structure of the hyperosmolality-gated calcium-permeable
1139 channel OSCA1.2. *Nat Commun* **9**:5060. doi:10.1038/s41467-018-07564-5

1140 López-Schier H, Hudspeth AJ. 2006. A two-step mechanism underlies the planar polarization
1141 of regenerating sensory hair cells. *Proc Natl Acad Sci U S A* **103**:18615–18620.
1142 doi:10.1073/pnas.0608536103

1143 Lukasz D, Kindt KS. 2018. In vivo calcium imaging of lateral-line hair cells in larval
1144 zebrafish. *J Vis Exp* **2018**:1–14. doi:10.3791/58794

1145 Maeda R, Kindt KS, Mo W, Morgan CP, Erickson T, Zhao H, Clemens-Grisham R, Barr-
1146 Gillespie PG, Nicolson T. 2014. Tip-link protein protocadherin 15 interacts with
1147 transmembrane channel-like proteins TMC1 and TMC2. *Proc Natl Acad Sci U S A*
1148 **111**:12907–12. doi:10.1073/pnas.1402152111

1149 Maeda R, Pacentine I V., Erickson T, Nicolson T. 2017. Functional analysis of the

1150 transmembrane and cytoplasmic domains of Pcdh15a in zebrafish hair cells. *J Neurosci*
1151 2216–16. doi:10.1523/JNEUROSCI.2216-16.2017

1152 McInturff S, Burns JC, Kelley MW. 2018. Characterization of spatial and temporal
1153 development of Type I and Type II hair cells in the mouse utricle using new cell-type-
1154 specific markers. *Biol Open* **7**:1–13. doi:10.1242/bio.038083

1155 Meyers JR, MacDonald RB, Duggan A, Lenzi D, Standaert DG, Corwin JT, Corey DP. 2003.
1156 Lighting up the Senses: FM1-43 Loading of Sensory Cells through Nonselective Ion
1157 Channels. *J Neurosci* **23**:4054–4065. doi:10.1523/JNEUROSCI.23-10-04054.2003

1158 Michel V, Booth KT, Patni P, Cortese M, Azaiez H, Bahloul A, Kahrizi K, Labbé M, Emptoz
1159 A, Lelli A, Dégardin J, Dupont T, Aghaie A, Oficjalska-Pham D, Picaud S, Najmabadi
1160 H, Smith RJ, Bowl MR, Brown SD, Avan P, Petit C, El-Amraoui A. 2017. CIB2,
1161 defective in isolated deafness, is key for auditory hair cell mechanotransduction and
1162 survival. *EMBO Mol Med* **9**:1711–1731. doi:10.15252/emmm.201708087

1163 Naz S, Giguere CM, Kohrman DC, Mitchem KL, Riazuddin Saima, Morell RJ, Ramesh A,
1164 Srisailpathy S, Deshmukh D, Riazuddin Sheikh, Griffith AJ, Friedman TB, Smith RJH,
1165 Wilcox ER. 2002. Mutations in a novel gene, TMIE, are associated with hearing loss
1166 linked to the DFNB6 locus. *Am J Hum Genet* **71**:632–636. doi:10.1086/342193

1167 Nicolson T. 2017. The genetics of hair-cell function in zebrafish. *J Neurogenet*.
1168 doi:10.1080/01677063.2017.1342246

1169 Nicolson T, Rüsch A, Friedrich RW, Granato M, Ruppersberg JP, Nüsslein-Volhard C. 1998.
1170 Genetic analysis of vertebrate sensory hair cell mechanosensation: The zebrafish circler
1171 mutants. *Neuron* **20**:271–283. doi:10.1016/S0896-6273(00)80455-9

1172 Nietlispach D. 2005. Suppression of anti-TROSY lines in a sensitivity enhanced gradient

1173 selection TROSY scheme. *J Biomol NMR* **31**:161–6. doi:10.1007/s10858-004-8195-7

1174 Norris M, Fetler B, Marchant J, Johnson BA. 2016. NMRFx Processor: a cross-platform
1175 NMR data processing program. *J Biomol NMR* **65**:205–216. doi:10.1007/s10858-016-
1176 0049-6

1177 Pan B, Akyuz N, Liu X-P, Asai Y, Nist-Lund C, Kurima K, Derfler BH, György B,
1178 Limapichat W, Walujkar S, Wimalasena LN, Sotomayor M, Corey DP, Holt JR. 2018.
1179 TMC1 Forms the Pore of Mechanosensory Transduction Channels in Vertebrate Inner
1180 Ear Hair Cells. *Neuron* **99**:736-753.e6. doi:10.1016/j.neuron.2018.07.033

1181 Phillips JB, Blanco-Sanchez B, Lentz JJ, Tallafuss A, Khanobdee K, Sampath S, Jacobs ZG,
1182 Han PF, Mishra M, Titus TA, Williams DS, Keats BJ, Washbourne P, Westerfield M.
1183 2011. Harmonin (Ush1c) is required in zebrafish Müller glial cells for photoreceptor
1184 synaptic development and function. *DMM Dis Model Mech* **4**:786–800.
1185 doi:10.1242/dmm.006429

1186 Phillips JC, Braun R, Wang W, Gumbart J, Tajkhorshid E, Villa E, Chipot C, Skeel RD, Kalé
1187 L, Schulten K. 2005. Scalable molecular dynamics with NAMD. *J Comput Chem*
1188 **26**:1781–1802. doi:10.1002/jcc.20289

1189 Pujol-Martí J, López-Schier H. 2013. Developmental and architectural principles of the
1190 lateral-line neural map. *Front Neural Circuits* **7**:1–9. doi:10.3389/fncir.2013.00047

1191 Qiu X, Liang X, Llongueras JP, Cunningham C, Müller U. 2023. The tetraspan LHFPL5 is
1192 critical to establish maximal force sensitivity of the mechanotransduction channel of
1193 cochlear hair cells. *Cell Rep* **42**:112245. doi:10.1016/j.celrep.2023.112245

1194 Riazuddin Saima, Belyantseva IA, Giese APJ, Lee K, Indzhykulian AA, Nandamuri SP,
1195 Yousaf R, Sinha GP, Lee S, Terrell D, Hegde RS, Ali RA, Anwar S, Andrade-Elizondo

1196 PB, Sirmaci A, Parise L V., Basit S, Wali A, Ayub M, Ansar M, Ahmad W, Khan SN,
1197 Akram J, Tekin M, Riazuddin Sheikh, Cook T, Buschbeck EK, Frolenkov GI, Leal SM,
1198 Friedman TB, Ahmed ZM. 2012. Alterations of the CIB2 calcium-and integrin-binding
1199 protein cause Usher syndrome type 1J and nonsyndromic deafness DFNB48. *Nat Genet*
1200 **44**:1265–1271. doi:10.1038/ng.2426

1201 Seco CZ, Giese AP, Shafique S, Schraders M, Oonk AMM, Grossheim M, Oostrik J, Strom
1202 T, Hegde R, Van Wijk E, Frolenkov GI, Azam M, Yntema HG, Free RH, Riazuddin S,
1203 Verheij JBGM, Admiraal RJ, Qamar R, Ahmed ZM, Kremer H. 2016. Novel and
1204 recurrent CIB2 variants, associated with nonsyndromic deafness, do not affect calcium
1205 buffering and localization in hair cells. *Eur J Hum Genet* **24**:542–549.
1206 doi:10.1038/ejhg.2015.157

1207 Seiler C, Ben-David O, Sidi S, Hendrich O, Rusch A, Burnside B, Avraham KB, Nicolson T.
1208 2004. Myosin VI is required for structural integrity of the apical surface of sensory hair
1209 cells in zebrafish. *Dev Biol* **272**:328–338. doi:10.1016/j.ydbio.2004.05.004

1210 Shaw DE, Grossman JP, Bank JA, Batson B, Butts JA, Chao JC, Deneroff MM, Dror RO,
1211 Even A, Fenton CH, Forte A, Gagliardo J, Gill G, Greskamp B, Ho CR, Ierardi DJ,
1212 Iserovich L, Kuskin JS, Larson RH, Layman T, Lee L-S, Lerer AK, Li C, Killebrew D,
1213 Mackenzie KM, Mok SY-H, Moraes MA, Mueller R, Nociolo LJ, Peticolas JL, Quan T,
1214 Ramot D, Salmon JK, Scarpazza DP, Schafer U Ben, Siddique N, Snyder CW, Spengler
1215 J, Tang PTP, Theobald M, Toma H, Towles B, Vitale B, Wang SC, Young C. 2014.
1216 Anton 2: Raising the Bar for Performance and Programmability in a Special-Purpose
1217 Molecular Dynamics SupercomputerSC14: International Conference for High
1218 Performance Computing, Networking, Storage and Analysis. IEEE. pp. 41–53.
1219 doi:10.1109/SC.2014.9

1220 Sheets L, He XJ, Olt J, Schreck M, Petralia RS, Wang YX, Zhang Q, Beirl A, Nicolson T,
1221 Marcotti W, Trapani JG, Kindt KS. 2017. Enlargement of ribbons in zebrafish hair cells
1222 increases calcium currents but disrupts afferent spontaneous activity and timing of
1223 stimulus onset. *J Neurosci* **37**:6299–6313. doi:10.1523/JNEUROSCI.2878-16.2017

1224 Shi T, Beaulieu MO, Saunders LM, Fabian P, Trapnell C, Segil N, Crump JG, Raible DW.
1225 2023. Single-cell transcriptomic profiling of the zebrafish inner ear reveals molecularly
1226 distinct hair cell and supporting cell subtypes. *Elife* **12**:1–24. doi:10.7554/eLife.82978

1227 Siemens J, Lillo C, Dumont R a, Reynolds A, Williams DS, Gillespie PG, Müller U. 2004.
1228 Cadherin 23 is a component of the tip link in hair-cell stereocilia. *Nature* **428**:950–955.
1229 doi:10.1038/nature02483

1230 Smith ET, Pacentine I, Shipman A, Hill M, Nicolson T. 2020. Disruption of tmc1/2a/2b
1231 Genes in Zebrafish Reveals Subunit Requirements in Subtypes of Inner Ear Hair Cells. *J*
1232 *Neurosci* **40**:4457–4468. doi:10.1523/JNEUROSCI.0163-20.2020

1233 Söllner C, Rauch G-J, Siemens J, Geisler R, Schuster SC, the Tübingen 2000 Screen
1234 Consortium, Müller U, Nicolson T. 2004. Mutations in cadherin 23 affect tip links in
1235 zebrafish sensory hair cells. *Nature* **428**:955–959. doi:10.1038/nature02484

1236 Sotomayor M, Weihofen WA, Gaudet R, Corey DP. 2012. Structure of a force-conveying
1237 cadherin bond essential for inner-ear mechanotransduction. *Nature* **492**:128–32.
1238 doi:10.1038/nature11590

1239 Sukharev S, Corey DP. 2004. Mechanosensitive channels: multiplicity of families and gating
1240 paradigms. *Sci STKE* **2004**:re4. doi:10.1126/stke.2192004re4

1241 Tunyasuvunakool K, Adler J, Wu Z, Green T, Zielinski M, Žídek A, Bridgland A, Cowie A,
1242 Meyer C, Laydon A, Velankar S, Kleywegt GJ, Bateman A, Evans R, Pritzel A,

1243 Figurnov M, Ronneberger O, Bates R, Kohl SAA, Potapenko A, Ballard AJ, Romera-
1244 Paredes B, Nikolov S, Jain R, Clancy E, Reiman D, Petersen S, Senior AW,
1245 Kavukcuoglu K, Birney E, Kohli P, Jumper J, Hassabis D. 2021. Highly accurate protein
1246 structure prediction for the human proteome. *Nature* 1–9. doi:10.1038/s41586-021-
1247 03828-1

1248 Vallone R, Dal Cortivo G, D'Onofrio M, Dell'Orco D. 2018. Preferential Binding of Mg2+
1249 Over Ca2+ to CIB2 Triggers an Allosteric Switch Impaired in Usher Syndrome Type 1J.
1250 *Front Mol Neurosci* **11**. doi:10.3389/fnmol.2018.00274

1251 Vanommeslaeghe K, MacKerell AD. 2015. CHARMM additive and polarizable force fields
1252 for biophysics and computer-aided drug design. *Biochim Biophys Acta* **1850**:861–871.
1253 doi:10.1016/j.bbagen.2014.08.004

1254 Varshney GK, Carrington B, Pei W, Bishop K, Chen Z, Fan C, Xu L, Jones M, LaFave MC,
1255 Ledin J, Sood R, Burgess SM. 2016. A high-throughput functional genomics workflow
1256 based on CRISPR/Cas9-mediated targeted mutagenesis in zebrafish. *Nat Protoc*
1257 **11**:2357–2375. doi:10.1038/nprot.2016.141

1258 Walujkar S, Lotthammer JM, Nisler CR, Sudar JC, Ballesteros A, Sotomayor M. 2021. In
1259 Silico Electrophysiology of Inner-Ear Mechanotransduction Channel TMC1 Models.
1260 *bioRxiv* 2021.09.17.460860. doi:10.1101/2021.09.17.460860

1261 Wang X, Liu S, Cheng Q, Qu C, Ren R, Du H, Li N, Yan K, Wang Y, Xiong W, Xu Z. 2023.
1262 CIB2 and CIB3 regulate stereocilia maintenance and mechanoelectrical transduction in
1263 mouse vestibular hair cells. *J Neurosci*. doi:10.1523/JNEUROSCI.1807-22.2023

1264 Wang Y, Li J, Yao X, Li W, Du H, Tang M, Xiong W, Chai R, Xu Z. 2017. Loss of CIB2
1265 causes profound hearing loss and abolishes mechanoelectrical transduction in mice.

1266 *Front Mol Neurosci* **10**. doi:10.3389/fnmol.2017.00401

1267 Waterhouse AM, Procter JB, Martin DMA, Clamp M, Barton GJ. 2009. Jalview Version 2--a
1268 multiple sequence alignment editor and analysis workbench. *Bioinformatics* **25**:1189–
1269 1191. doi:10.1093/bioinformatics/btp033

1270 Xiong W, Grillet N, Elledge HM, Wagner TFJ, Zhao B, Johnson KR, Kazmierczak P, Müller
1271 U. 2012. TMHS is an integral component of the mechanotransduction machinery of
1272 cochlear hair cells. *Cell* **151**:1283–95. doi:10.1016/j.cell.2012.10.041

1273 Zhang M, Wang D, Kang Y, Wu J-X, Yao F, Pan C, Yan Z, Song C, Chen L. 2018. Structure
1274 of the mechanosensitive OSCA channels. *Nat Struct Mol Biol* **25**:850–858.
1275 doi:10.1038/s41594-018-0117-6

1276 Zhang Q, Li S, Wong HTC, He XJ, Beirl A, Petralia RS, Wang YX, Kindt KS. 2018.
1277 Synaptically silent sensory hair cells in zebrafish are recruited after damage. *Nat*
1278 *Commun* **9**:1–16. doi:10.1038/s41467-018-03806-8

1279 Zhao H, Williams DE, Shin J-B, Brügger B, Gillespie PG. 2012. Large membrane domains in
1280 hair bundles specify spatially constricted radixin activation. *J Neurosci* **32**:4600–9.
1281 doi:10.1523/JNEUROSCI.6184-11.2012

1282 Zhu J, Xu H, Song H, Li X, Wang N, Zhao J, Zheng X, Kim KY, Zhang H, Mao Q, Xia H.
1283 2021. CRISPR/Cas9-mediated grna gene knockout leads to neurodevelopmental defects
1284 and motor behavior changes in zebrafish. *J Neurochem* **157**:520–531.
1285 doi:10.1111/jnc.15307

1286

1287

1288 **Figures and figure legends**

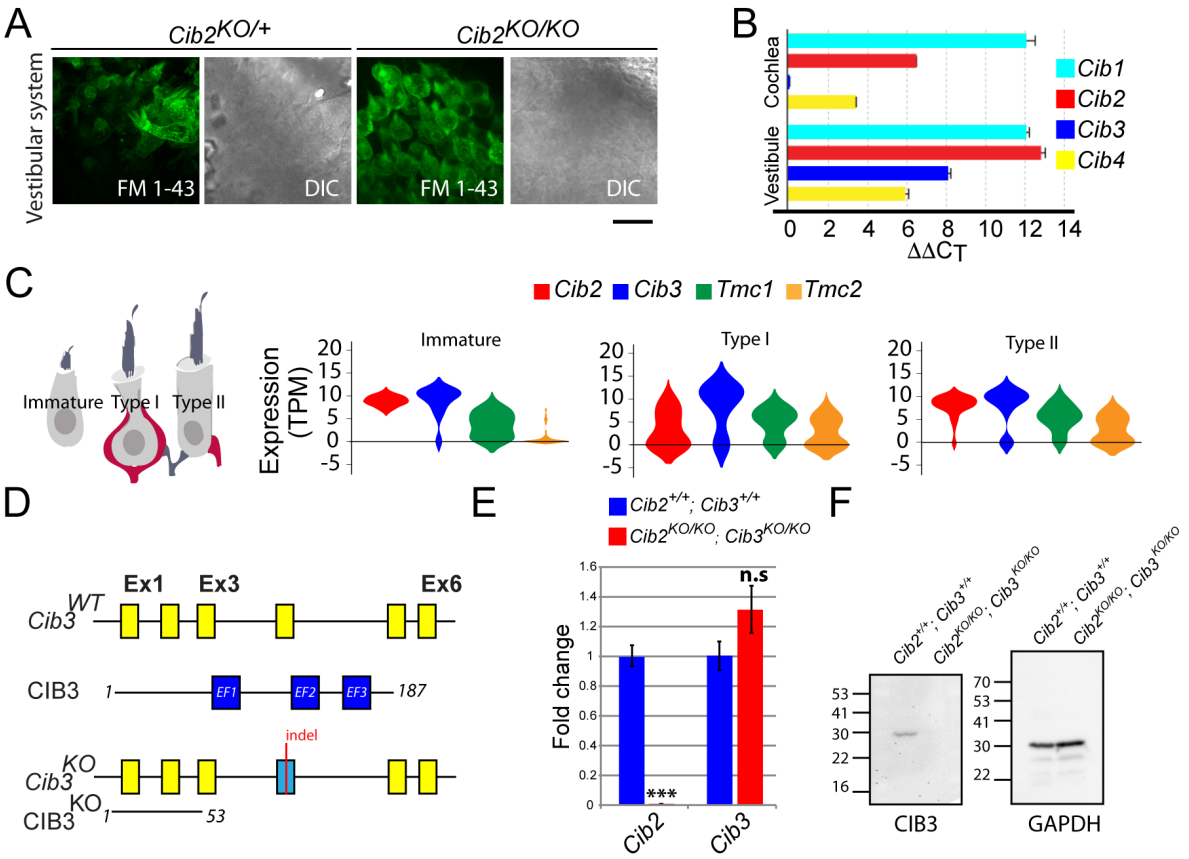

1289

1290 **Figure 1. Expression of *Cib* genes in the mouse inner ear and generation of *Cib3* knockout**
1291 **mice.** (**A**) Maximum intensity projections of Z-stacks of confocal fluorescent images and
1292 corresponding DIC images of *Cib2*$^{KO/+}$ and *Cib2*$^{KO/KO}$ cultured vestibular end organ explants
1293 imaged after exposure to 3 µM of FM 1-43 for 10 s. The samples were dissected at P5 and kept
1294 2 days *in vitro* (P5 + 2div). Scale bar: 20 µm. (**B**) Real-time quantitative RT–PCR analysis of
1295 mRNA levels in the cochlear and vestibular sensory epithelia at P12 revealed different
1296 expression of *Cib1*, *Cib2*, *Cib3,* and *Cib4* in the auditory and vestibular end organs. (**C**) Violin
1297 plots generated by gEAR portal showing the expression levels of *Cib2*, *Cib3*, *Tmc1,* and *Tmc2*
1298 by scRNA-seq in immature, type 1, and type 2 utricular vestibular hair cells. TPM: transcript
1299 per million. (**D**) Gene structure of the wild-type and *Cib3*^{KO} alleles. Exons are shown in yellow.
1300 Indel in exon 4 leads to a nonsense mutation and a premature stop at the protein level (p.

1301 Asp54*) (**E**) Real-time quantitative RT–PCR analysis using cDNA from brain tissue of
1302 *Cib2;Cib3* mutant mice was used to analyze the expression of *Cib2* and *Cib3*. Contrary to *Cib2*
1303 mRNA, *Cib3* mRNA appears to be stable in the $Cib2^{KO/KO};Cib3^{KO/KO}$ mice and does not go
1304 through nonsense mediated decay process. The relative expression of *Cib2* and *Cib3* members
1305 were normalized against *hprt*. Asterisks indicate statistical significance: ***, $p<0.001$
1306 (Student's t-test). n.s.: not significant. Error bars represent SEM. (**F**) Western Blot analysis on
1307 *Cib2;Cib3* mouse heart tissue was performed using CIB3 antibody. No CIB3 protein was
1308 detected in the $Cib2^{KO/KO};Cib3^{KO/KO}$ mice, validating our mouse model. GAPDH detection was
1309 used as a loading control.
1310
1311

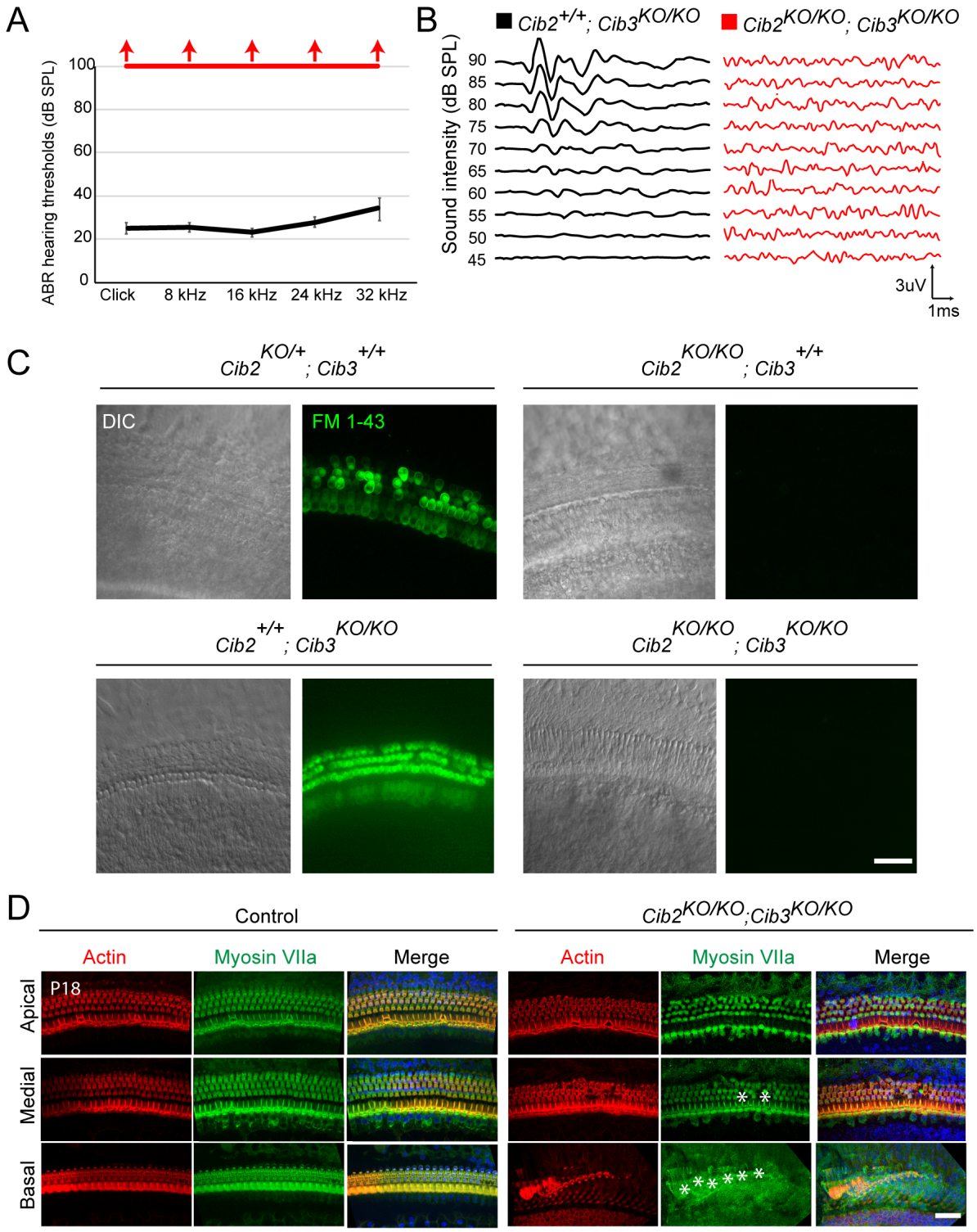

1312

1313 **Figure 2. CIB2/3 double mutant mice have profound hearing loss.** (**A**) ABR thresholds to

1314 broadband clicks and tone-pips with frequencies of 8 kHz, 16 kHz, 24 kHz and 32 kHz in

1315 *Cib2*$^{+/+}$;*Cib3*$^{KO/KO}$ (black; n = 5) and *Cib2*$^{KO/KO}$;*Cib3*$^{KO/KO}$ (red, n = 5) mice at P16. The same
1316 animals were tested with clicks and tone pips. (**B**) ABR pure tone traces of P32
1317 *Cib2*$^{+/+}$;*Cib3*$^{KO/KO}$ (black) and *Cib2*$^{KO/KO}$;*Cib3*$^{KO/KO}$ (red) mice measured at 32 kHz. Hearing
1318 thresholds are in Decibels (dB SPL). (**C**) Maximum intensity projections of Z-stacks of
1319 confocal fluorescent images (right) and corresponding DIC images (left) of *Cib2*$^{KO/+}$;*Cib3*$^{+/+}$,
1320 *Cib2*$^{KO/KO}$;*Cib3*$^{+/+}$, *Cib2*$^{+/+}$;*Cib3*$^{KO/KO}$ and *Cib2*$^{KO/KO}$;*Cib3*$^{KO/KO}$ cultured organ of Corti
1321 explants imaged after exposure to 3 µM of FM 1-43 for 10 s. The samples were dissected at P5
1322 and kept 2 days in vitro (P5 + 2div). Scale bar: 20 µm. (**D**) Maximum intensity projections of
1323 confocal Z-stacks of apical, medial and basal turns of organ of Corti of control and
1324 *Cib2*$^{KO/KO}$;*Cib3*$^{KO/KO}$ mice immunostained with an anti-myosin VIIa antibody (green) and
1325 counterstained with phalloidin (red) at P18. Asterisks indicate hair cell loss. Scale bar: 10 µm.
1326
1327

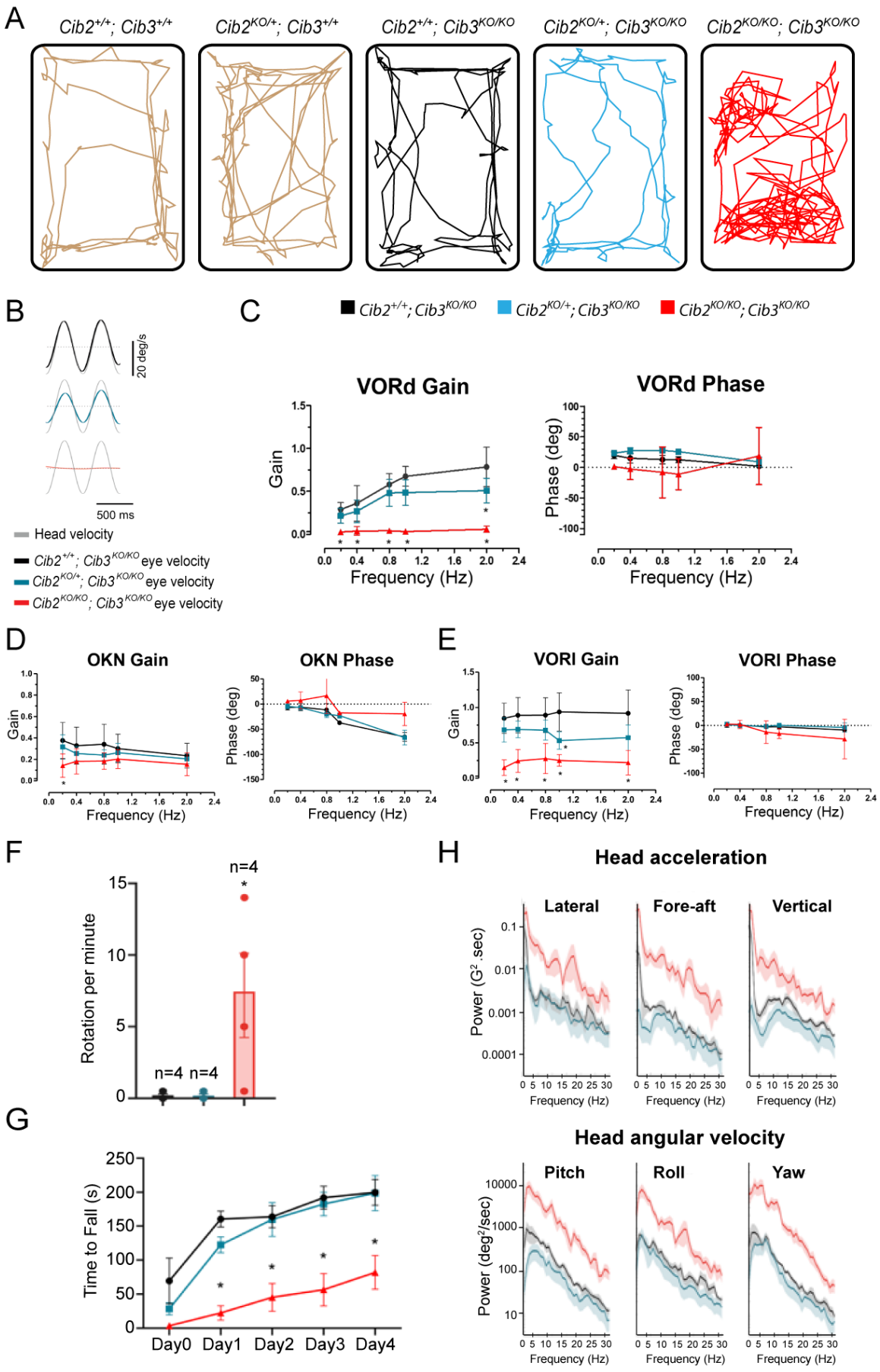
A
Cib2+/+; Cib3+/+
Cib2KO/+; Cib3+/+
Cib2+/+; Cib3KO/KO
Cib2KO/+; Cib3KO/KO
Cib2KO/KO; Cib3KO/KO
B
20 deg/s
500 ms
Head velocity
Cib2+/+; Cib3KO/KO eye velocity
Cib2KO/+; Cib3KO/KO eye velocity
Cib2KO/KO; Cib3KO/KO eye velocity
C
Cib2+/+; Cib3KO/KO
Cib2KO/+; Cib3KO/KO
Cib2KO/KO; Cib3KO/KO
VORd Gain
Gain
Frequency (Hz)
VORd Phase
Phase (deg)
Frequency (Hz)
D
OKN Gain
Gain
Frequency (Hz)
OKN Phase
Phase (deg)
Frequency (Hz)
E
VORI Gain
Gain
Frequency (Hz)
VORI Phase
Phase (deg)
Frequency (Hz)
F
Rotation per minute
n=4
n=4
n=4
G
Time to Fall (s)
Day0
Day1
Day2
Day3
Day4
H
Head acceleration
Lateral
Fore-aft
Vertical
Power (G2.sec)
Frequency (Hz)
Head angular velocity
Pitch
Roll
Yaw
Power (deg2/sec)
Frequency (Hz)

1328

1329 **Figure 3. CIB2/3 double mutant mice have vestibular dysfunction.** (**A**) Traces showing the
1330 open-field exploratory behavior of P60 *Cib2*$^{+/+}$*;Cib3*$^{+/+}$*, Cib2*$^{KO/+}$*;Cib3*$^{+/+}$*, Cib2*$^{+/+}$*;Cib3*$^{KO/KO}$,
1331 *Cib2*$^{KO/+}$*;Cib3*$^{KO/KO}$ and *Cib2*$^{KO/KO}$*;Cib3*$^{KO/KO}$ mutant mice. (**B**) Examples of head-velocity
1332 (grey) and resultant eye-velocity traces evoked during VORd testing. Note, the eye movement
1333 is compensatory, and the trace has been inverted to facilitate comparison with head velocity.
1334 (**C**) VORd Gain and phase (mean ± SD) plotted as a function of frequency for
1335 *Cib2*$^{+/+}$*;Cib3*$^{KO/KO}$ (n = 4), *Cib2*$^{KO/+}$*;Cib3*$^{KO/KO}$ (n = 5), *Cib2*$^{KO/KO}$*;Cib3*$^{KO/KO}$ (n = 4). (**D**) OKN
1336 gain and phase (mean ± SD) plotted as a function of frequency for *Cib2*$^{+/+}$*; Cib3*$^{KO/KO}$ (n = 4),
1337 *Cib2*$^{KO/+}$*;Cib3*$^{KO/KO}$ (n = 5), *Cib2*$^{KO/KO}$*;Cib3*$^{KO/KO}$ (n = 4). (**E**) VORl gain and phase (mean ±
1338 SD) plotted as a function of frequency for *Cib2*$^{+/+}$*;Cib3*$^{KO/KO}$ (n = 4), *Cib2*$^{KO/+}$*;Cib3*$^{KO/KO}$ (n =
1339 5), *Cib2*$^{KO/KO}$*;Cib3*$^{KO/KO}$ (n = 4). Comparisons made with two-way ANOVA followed by
1340 Bonferroni post-hoc test for (A-D); *$p < 0.05$. (**F**) Quantification of the number of rotations in
1341 120 seconds (mean ± SEM), showing that, unlike *Cib2*$^{+/+}$*;Cib3*$^{KO/KO}$, and *Cib2*$^{KO/+}$*;Cib3*$^{KO/KO}$
1342 mice, *Cib2*$^{KO/KO}$*;Cib3*$^{KO/KO}$ mutant mice display a circling behavior and a vestibular defect (*t*-
1343 test) (n = 4 for each genotype). (**G**) Quantification of the time mice remained on the rotating
1344 rod with increasing acceleration (mean ± SEM). Comparisons made with two-way ANOVA
1345 followed by Bonferroni post-hoc test for (F-K); *P<0.002. (*Cib2*$^{+/+}$*;Cib3*$^{KO/KO}$ (n = 6),
1346 *Cib2*$^{KO/+}$*;Cib3*$^{KO/KO}$ (n = 6), *Cib2*$^{KO/KO}$*;Cib3*$^{KO/KO}$ (n = 6)). (**H**) Comparison of power spectra
1347 density of head movements in translational axes (top) and rotational axes (bottom) between
1348 wild type (*Cib2*$^{+/+}$*;Cib3*$^{KO/KO}$*,* black), heterozygous mutants (*Cib2*$^{KO/+}$*;Cib3*$^{KO/KO}$, blue), and
1349 homozygous mutants (*Cib2*$^{KO/KO}$*;Cib3*$^{KO/KO}$, red). The double knockout *Cib2*$^{KO/KO}$*;Cib3*$^{KO/KO}$
1350 exhibit significantly higher power than *Cib2*$^{+/+}$*;Cib3*$^{KO/KO}$ *and Cib2*$^{KO/+}$*;Cib3*$^{KO/KO}$ across all
1351 frequencies (0–30 Hz), in all six translational and rotational axes.
1352

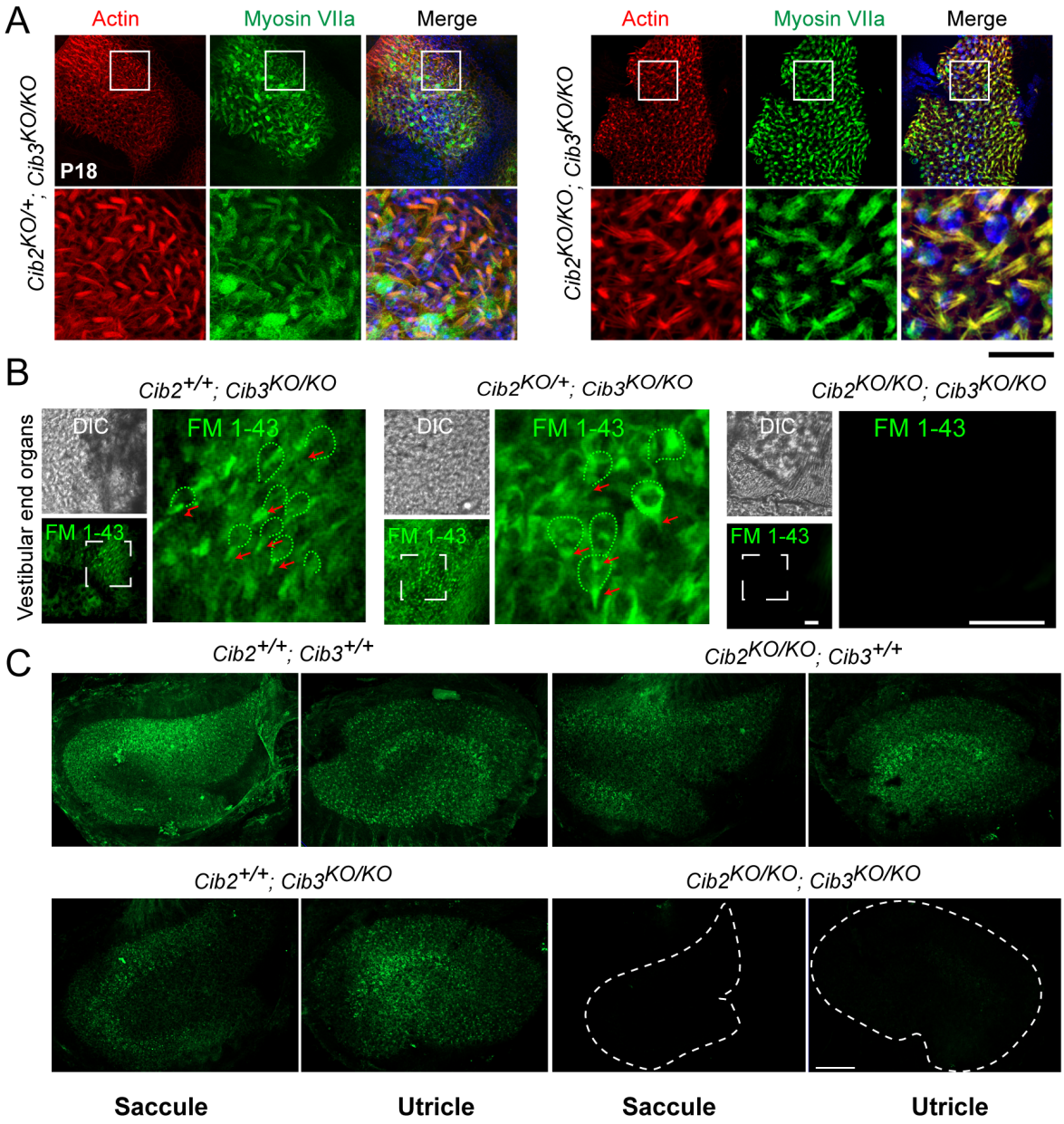

1353

1354 **Figure 4. Vestibular hair cells do not have functional MET channels at rest in CIB2/3**
1355 **double mutant mice.** (**A**) Maximum intensity projections of confocal Z-stacks of the
1356 vestibular end organs of P18 *Cib2*$^{KO/+}$;*Cib3*$^{KO/KO}$ and *Cib2*$^{KO/KO}$;*Cib3*$^{KO/KO}$ mutant mice
1357 immunostained with myosin VIIa antibody (green) and counterstained with phalloidin (red)
1358 and DAPI (blue). Scale bar = 50 µm. (**B**) Adult vestibular end organs of *Cib2*$^{+/+}$;*Cib3*$^{KO/KO}$,
1359 *Cib2*$^{KO/+}$;*Cib3*$^{KO/KO}$ and *Cib2*$^{KO/KO}$;*Cib3*$^{KO/KO}$ mutant mice imaged after exposure to 3 µM of
1360 FM 1-43 for 10 s. Vestibular hair cell bodies (green doted lines), and stereocilia bundles (red

1361 arrows) are shown. Scale bar: 100 µm. (**C**) FM 1-43FX (fixable form) labeling of saccules and

1362 utricles by IP injection at P60. Obvious reduction in signal in *Cib2*$^{KO/KO}$;*Cib3*$^{KO/KO}$, and subtle

1363 extrastriolar reduction in *Cib2*$^{+/+}$;*Cib3*$^{KO/KO}$ mice was observed. Scale bar = 100 µm.

1364

1365

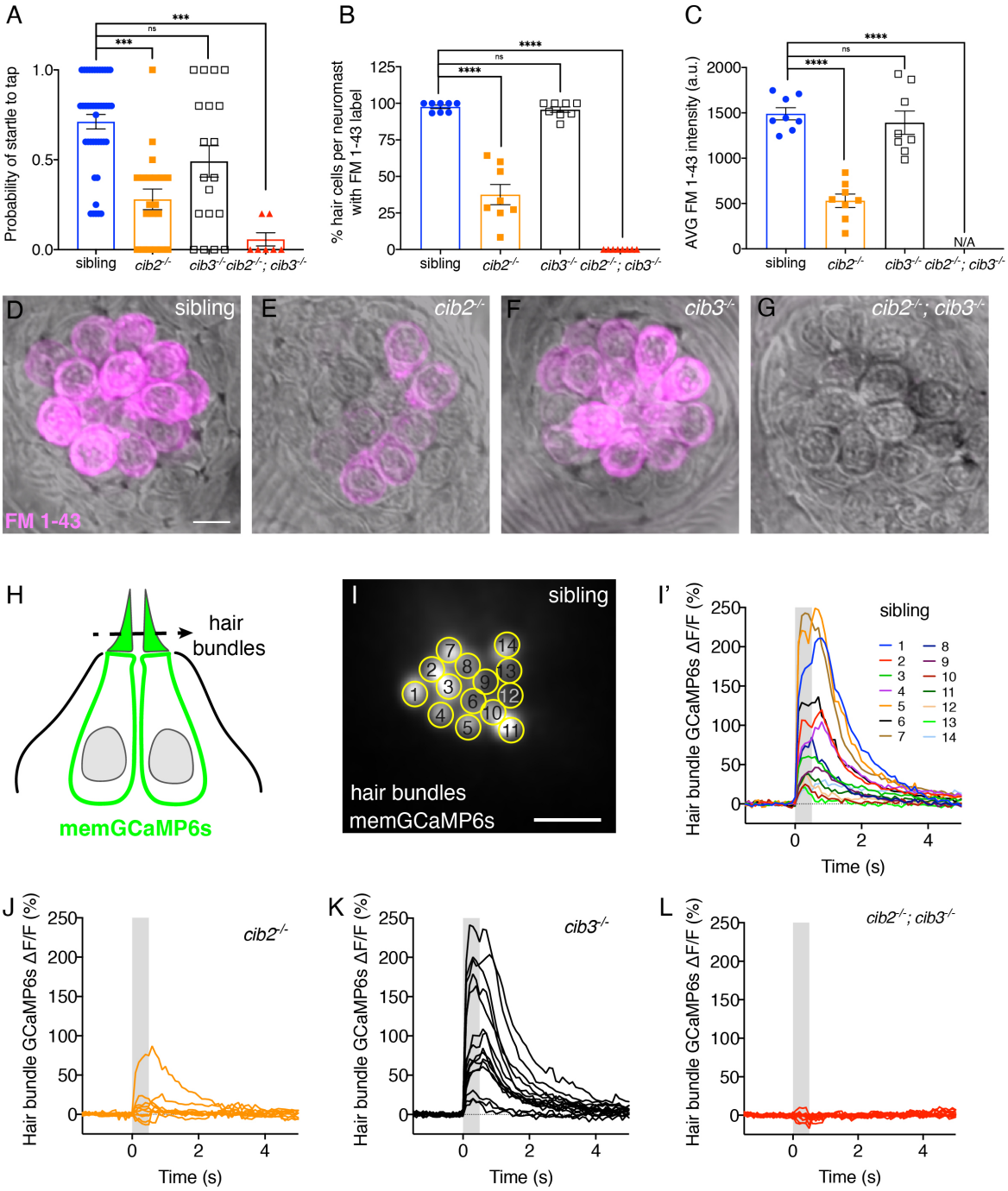

Figure 5. Both Cib2 and Cib3 are required in zebrafish for acoustic startle and MET function. (**A**) Compared to controls (siblings) *cib3* mutants have a normal acoustic startle response. *Cib2;cib3* double mutants completely lack an acoustic startle response, while *cib2* mutants have a reduced probability to startle compared to controls (n = 43 sibling, 20 *cib2*, 19 *cib3* and 7 *cib2;cib3* animals). (**B**) Compared to controls *cib3* mutants have a normal % of hair

1372 cells that label with FM 1-43 per neuromast. In *cib2;cib3* mutants no hair cells label with FM
1373 1-43, and in *cib2* mutants a significantly reduced % of hair cells label with FM 1-43 per
1374 neuromast. (**C**) The average intensity of FM 1-43 labeling in *cib3* mutant hair cells is similar
1375 to controls. In contrast, in *cib2* mutants, hair cells that label with FM 1-43, have a significantly
1376 reduced intensity compared to controls (n = 8 neuromasts per genotype in B and C). (**D-G**)
1377 Representative neuromasts labeled with FM 1-43 for each genotype. FM 1-43 label is overlaid
1378 onto laser scanning DIC images. (**H**) Schematic showing the localization of membrane-
1379 localized GCaMP6s (memGCaMP6s); the indicator used to measure Ca^{2+} influx into lateral-
1380 line hair bundles. The plane used for Ca^{2+} imaging and to determine if a hair cell is
1381 mechanosensitive is indicated by the dashed arrow. (**I-I'**) Representative example of a hair
1382 bundle imaging plane (I), along with the resulting Ca^{2+} responses (I') from hair bundles from
1383 a control neuromast. The ROIs used to measure Ca^{2+} signals in each hair bundle are indicated
1384 in (I). (**J-L**) Representative examples of Ca^{2+} responses from neuromasts in *cib2* (J), *cib3* (K)
1385 and *cib2;cib3* mutants (L). FM 1-43 imaging and behavior were performed at 5 dpf. Ca^{2+}
1386 imaging was performed at 5 or 6 dpf. A Kruskal-Wallis test was used in A; A one-way ANOVA
1387 was used in B and C. The scale bar in D and I = 5 µm. The online version of this article includes
1388 source data and the following figure supplement(s) for Figure 5.
1389
1390 **Figure supplement 1.** Summary of mechanosensitive Ca^{2+} responses in zebrafish.
1391
1392

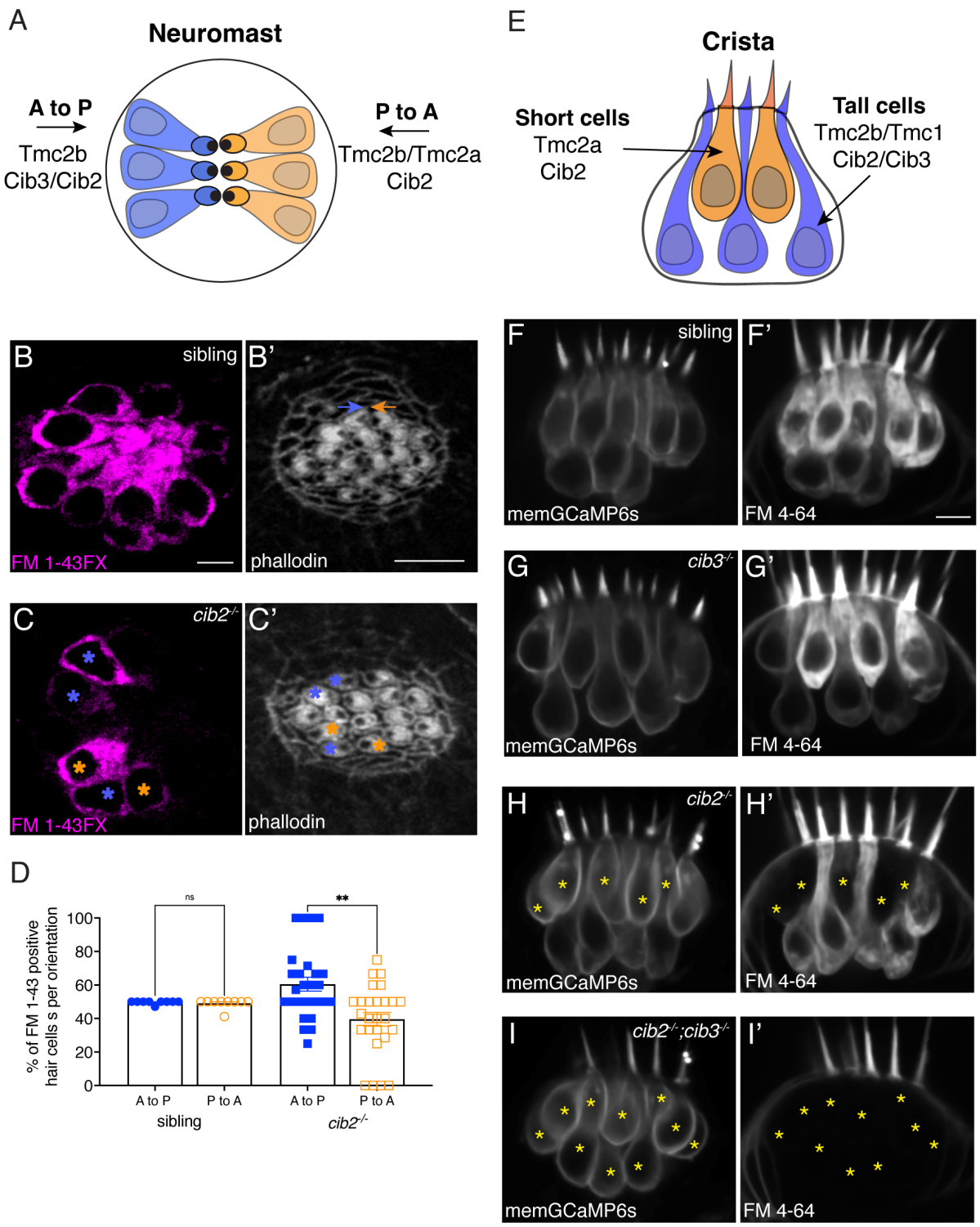

Figure 6. Cib2 is required in specific subsets of hair cells in the zebrafish pLL and inner ear. (**A**) Overview of Tmc requirements in pLL hair cells. Hair cells that sense posterior flow (orange) rely on Tmc2b, while hair cells that sense anterior flow (blue) can rely on Tmc2b and/or Tmc2a for mechanosensitive function. (**B-C'**) FM 1-43FX labeling in pLL neuromasts

1398 from sibling control (B) and *cib2* mutants (C). The residual cells in *cib2* mutants rely on Cib3
1399 for mechanosensitive function. Phalloidin label can be used to link FM 1-43FX label to the
1400 orientation of pLL hair cells (C,C'; see colored asterisks). In B', orange and blue arrows rest
1401 above hair cells that are oriented to respond to anterior and posterior flow, respectively. (**D**)
1402 Quantification reveals that a similar percentage of anterior and posterior responsive pLL hair
1403 cells label with FM 1-43FX in sibling controls (posterior flow: 49.7 %, anterior flow: 49.2 %,
1404 n = 9 neuromasts). In contrast, in *cib2* mutants, a significantly higher percentage of posterior
1405 responsive pLL hair cells label with FM 1-43FX in *cib2* mutants (posterior flow: 60.5 %,
1406 anterior flow: 39.5 %, n = 26 neuromasts). (**E**) Overview of Tmc and Cib requirements in the
1407 hair cells of zebrafish cristae. Short teardrop-shaped cells rely primarily on Tmc2a, while tall
1408 gourd-shaped cells rely primarily on Tmc2b and Tmc1. (**F-I'**) Medial cristae for each genotype.
1409 MemGCaMP6s labels all hair cells, while FM 4-64 labels hair cells with intact
1410 mechanosensitive function. In siblings and *cib3* mutants, both teardrop and gourd cells label
1411 with FM 4-64 (F-F', G-G'). In *cib2;cib3* double mutants, no hair cells label with FM 4-64
1412 (asterisks) (I-I'). In *cib2* mutants many short cells fail to label with FM 4-64 (asterisks) (H-H'),
1413 (n = 13 double het sibling, 7 *cib3*, 14 *cib2* and 4 double mutant crista). All images were acquired
1414 at 5 dpf. A Kruskal-Wallis test was used in D; $P > 0.01$. The scale bars in B, B', and F' = 5
1415 µm.
1416
1417

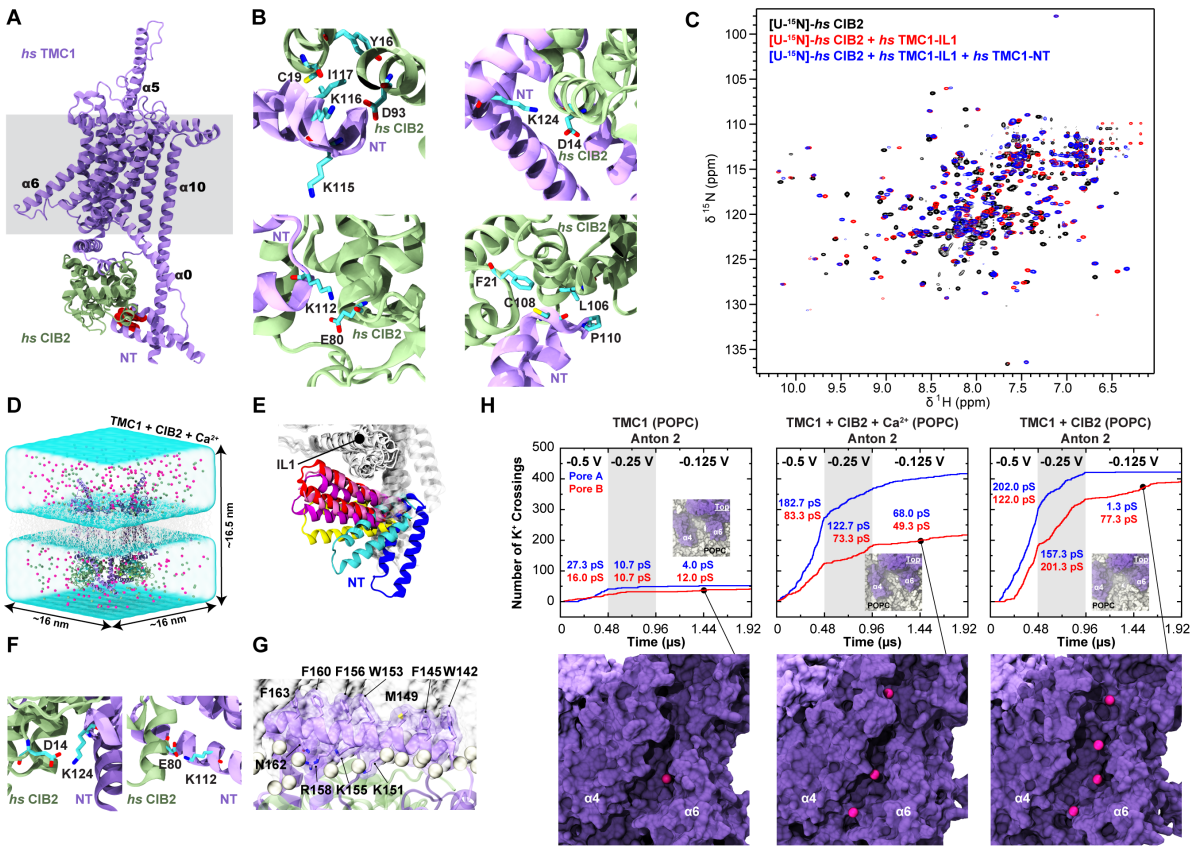

Figure 7. AF2 predictions, NMR data, and simulations support a clamp-like model for the human TMC1 and CIB2 complex. (**A**) AF2 model of *hs* TMC1 in complex with *hs* CIB2. Side view of monomeric *hs* TMC1 (light purple) in complex with *hs* CIB2 (light sea green). N-terminal residues of TMC1 known to interact with CIB2 are in red. (**B**) Top left panel shows residues at the *hs* TMC1-NT fragment (115-117) shown to weaken interaction with CIB2 upon mutation (Liang et al., 2021) at the interface with CIB2. Additional panels show details of contacts between TMC1 and CIB2 with formation of K124:D14 and K112:E80 salt bridges, as well as hydrophobic interactions. (**C**) Overlay of ^{1}H-^{15}N TROSY-HSQC spectra of *hs* [U-^{15}N]-CIB2 (black) alone and bound to either only *hs* TMC1-IL (red) or both *hs* TMC1-IL and *hs* TMC1-NT (blue). (**D**) A complete simulation system of *hs* TMC1 in complex with *hs* CIB2-Ca^{2+} is shown in surface representation. *hs* TMC1 is shown in light (monomer A) and dark (monomer B) purple, *hs* CIB2 in light sea green, water in transparent light blue, lipid membrane

1431 in gray lines, and K^+ and Cl^- ions are shown as pink and green spheres, respectively. (**E**) The
1432 *hs* TMC1-NT domain explores diverse conformational space in the absence of CIB during
1433 equilibrium simulations (S3a). (**F**) Salt bridges K124:D14 and K112:E80 remain throughout
1434 equilibrium simulations. (**G**) snapshot of amphipathic helix α0 inserting into the lipid bilayer
1435 (S4c). (**H**) Number of K^+ crossings as a function of time for pores A and B of *hs* TMC1, *hs*
1436 TMC1 + *hs* CIB2 + Ca^{2+}, and *hs* TMC1 + *hs* CIB2 in a POPC bilayer at -0.5 V, -0.25 V, and -
1437 0.125 V. Insets show top views of pore region with TMC1 (dark purple) and lipids (light gray)
1438 in surface representation (protein and lipids partially excluded for clarity). Representative
1439 images of K^+ permeating the pore region between α4 and α6 of *hs* TMC1 are shown with
1440 protein in surface representation and ions as pink spheres. Conductance values calculated for
1441 K^+ crossings.
1442 The online version of this article includes source data and the following figure supplement(s)
1443 for Figure 7.
1444 **Figure supplement 1.** Overview of TMC1/2 and CIB2/3 AF2 models.
1445 **Figure supplement 2.** TMC sequence alignment.
1446 **Figure supplement 3.** CIB2 sequence alignment.
1447 **Figure supplement 4.** CIB3 sequence alignment.
1448 **Figure supplement 5.** CIB sequence alignment.
1449 **Figure supplement 6.** SEC of *hs* CIB2 and *hs* CIB3 either refolded alone or co-refolded with *hs*
1450 TMC1-IL1, and *hs* TMC1-NT
1451 **Figure supplement 7.** ^1H-^{15}N TROSY-HSQC spectra.
1452 **Figure supplement 8.** Stability of TMC/CIB complexes, monomers, and subdomains.
1453 **Figure supplement 9.** BSA in *hs* TMC1/2 and *hs* CIB2/3 complexes.
1454 **Figure supplement 10.** Number of K^+ crossings as a function of time for pores A and B of *hs* TMC1
1455 and *hs* TMC2.

1456 **Figure supplement 11.** Conduction events in long timescale simulations and summary of predicted

1457 conductance values.

1458 **Figure supplement 12.** Possible combinations of TMC1, TMC2, CIB2, and CIB3 complexes.

1459 **Figure 7-video 1.** Overview of *hs* TMC1 (light and dark purple) in complex with *hs* CIB2
1460 (light sea green)-Ca^{2+} (green spheres). K^+ ions (pink) were shown to be permeating the pore
1461 region between α4 and α6. Water molecules, lipids, and protein side chains were omitted for
1462 clarity.
1463

1464 **Figure 7-video 2.** Side view of the *hs* TMC1 channel pore during a trajectory at -0.5 V
1465 (monomer B). K^+ (pink) are seen permeating the pore from one side (S1b); *hs* TMC1 (monomer
1466 B) is shown in dark purple and *hs* CIB2 is shown in light sea green. Water molecules, lipids,
1467 *hs* TMC1 (monomer A), and protein side chains were omitted for clarity.
1468

1469